

The XMM-Newton Serendipitous Survey

III. The SSC survey of the Galactic plane[★]

C. Motch¹, X. Barcons², F. Carrera², M. S. Cropper³, P. Guillout¹, J.-M. Hameury¹, O. Herent¹, A. Martocchia^{1,7}, L. Michel¹, M.W. Pakull¹, T. P. Roberts⁴, S. Rosen³, A. Schwobe⁵, G. P. Szokoly⁶, J. Tedds⁴, R. Warwick⁴, M. Watson⁴, N. A. Webb⁷, and P. J. Wheatley⁴

(Affiliations can be found after the references)

Received date will be inserted by the editor; accepted date will be inserted by the editor

ABSTRACT

We report first results from a project carried out by the Survey Science Centre of the XMM-Newton satellite aiming at the optical identification and characterisation of serendipitous EPIC sources at low galactic latitudes ($|b| < 20^\circ$). The present study focusses on a group of 9 XMM-Newton fields containing 411 sources and covering a total area of 1.8 deg^2 . We reach typical sensitivities of $\sim 3 \cdot 10^{-15} \text{ erg cm}^{-2} \text{ s}^{-1}$ in the 0.5 to 2.0 keV soft band and of $\sim 3 \cdot 10^{-14} \text{ erg cm}^{-2} \text{ s}^{-1}$ in the 2.0 to 12.0 keV hard band. Deep multi-colour optical imaging and spectroscopy have been obtained in the framework of the AXIS project and from other programs at the CFHT, ESO and the OHP. These observations have led to a number of optical identifications, mainly with active stars, but also with a small number of accreting sources or accreting candidates, one CV and 3 Be stars. We argue that this group of Be stars has optical and X-ray properties very similar to those of γ -Cas and could thus either be accreting white dwarfs or particularly active magnetic stars. The surface density of identified active coronae sharply drops by a factor of ~ 2 when moving from $b = 0^\circ$ to 14° and by a factor of ~ 5 when reaching $b = 50^\circ$. The X-ray stellar population model accounts remarkably well for the observed $\log N(>S)$ - $\log S$ curves for identified active coronae once the variation of the mean local absorption and biases introduced by the limiting magnitude for optical identification are taken into account. At mid galactic latitudes ($|b| < 3^\circ$ - 16°), a small fraction of the extragalactic population is bright enough in the optical to be detected with our instrumentation. In this range of latitudes, the AGN population dominates X-ray number counts at all energies being most prominent in the hard X-rays. At very low latitudes ($b \sim 0$), active coronae account for the totality of the soft (0.5-2.0 keV) source counts. In the hard band (2.0-12.0 keV), we find a clear excess of sources above the expected extragalactic contribution. This galactic population of relatively low X-ray luminosity ($L_X \sim 10^{33} \text{ erg s}^{-1}$) is seen at $l = -50^\circ$ and $l = 10$ - 20° but is mostly apparent in the very central parts of the Galaxy. Using additional XMM-Newton observations, we argue that the density of hard sources seen toward the galactic center may steeply drop when moving away from $b = 0^\circ$ to $|b| = 0.3^\circ$. This strong gradient is consistent with a source population located in the nuclear bulge.

1. Introduction

Thanks to their excellent sensitivity, good image quality over a wide field of view ($30'$) and wide energy range (0.2-12 keV) the EPIC cameras on board XMM-Newton allow X-ray surveys

with an unprecedented combination of large area and depth. This potential was recognised by ESA in setting up a dedicated XMM-Newton Survey Science Center (SSC) to facilitate the exploitation of the XMM-Newton Serendipitous Sky Survey by providing a public archive of data products and carrying out a carefully coordinated follow-up programme to characterise the overall X-ray source population (Watson et al. 2001).

Send offprint requests to: C. Motch

[★] Based on observations carried out at the European Southern Observatory, La Silla and Paranal, Chile under program Nos 69.D-0143, 70.D-0227, 71.D-0296, 71.D-0552. Based on observations obtained at the Canada-France-Hawaii Telescope (CFHT) which is operated by the National Research Council of Canada, the Institut National des Sciences de l'Univers of the Centre National de la Recherche Scientifique of France, and the University of Hawaii. Based on Observations obtained at the Observatoire de Haute Provence which is operated by the Centre National de la Recherche Scientifique of France. Based on observations obtained with XMM-Newton, an ESA science mission with instruments and contributions directly funded by ESA Member States and NASA.

In this paper we present results from an ongoing optical identification campaign conducted at low galactic latitudes by the SSC of the XMM-Newton satellite. The XMM-Newton SSC Galactic Plane Survey aims at providing a reference frame for the characterisation of all low galactic latitude ($|b| \leq 20^\circ$) EPIC serendipitous point-like source detections. The project does not directly address the nature of the various diffuse emission components encountered in galactic fields. It can however shed light on the possibility that some apparently diffuse structures such as the Galactic Ridge are due to unresolved popu-

lations of faint sources. Preliminary results were presented in Motch et al. (2000, 2002 and 2003).

The XMM-Newton SSC Galactic Plane Survey uses several distinct strategies to describe the source content of the XMM-Newton low galactic fields. The first part of the project, which is the scope of this paper, consists of trying to identify all sources detected in several deep fields selected to cover representative directions of the Galaxy. A second program aims at identifying X-ray bright sources all over the Galaxy, including the XGPS (Hands et al. 2004) survey. The goal of the third project is to study the properties of the optically bright ($R < 17$) stellar population in a rather large number of XMM-Newton observations (17 fields amounting to $\sim 3 \text{ deg}^2$) using easily accessible 2m-class telescopes. A final program consists of the identification of X-ray sources selected on the basis of their X-ray and optical properties.

Beyond proper identification and classification, our objective is to study source properties, quantify their relative contributions to the overall soft and hard X-ray galactic emission. XMM-Newton measurements are not strongly biased by interstellar extinction, as were earlier studies based on ROSAT observations restricted to the softer 0.1-2.4 keV band. Although similar in X-ray flux to the deepest ROSAT pointings, the galactic landscape unveiled by XMM-Newton differs from that seen by ROSAT. Opening new parameter spaces the present survey offers the possibility to reveal completely new classes of sources.

Many individual source types are known to contribute to the galactic X-ray source demography in the medium to low X-ray luminosity regime ($10^{28-36} \text{ erg s}^{-1}$). These include, late and early-type stars, cataclysmic variables (CVs), RS CVns and various species of X-ray binaries. Other kinds of rare emitters such as isolated neutron stars, isolated black holes or low-luminosity but long-lived evolutionary states of classical XRBs may be found. Pre low-mass X-ray binaries, i.e. systems consisting of a late type star and a wind accreting neutron star will have X-ray luminosities of the order of $10^{31} \text{ erg s}^{-1}$ and could be as numerous as 10^4 or 10^5 in the Galaxy (Willems & Kolb 2003). In general, neutron stars accreting from the wind of a main sequence companion may be in equally large numbers and could be dominated by intermediate mass primaries ($M = 3-8 M_{\odot}$) (Pfahl et al. 2002). Only a fraction of these systems will evolve into a high X-ray luminosity stage. All known Be/X-ray binaries display direct evidence (pulsations) or indirect evidence (X-ray spectra) of an accreting neutron star (Negueruela 1998). The large mass transfer which may occur during the evolution of the primary star can lead to the creation of a white dwarf (WD) remnant instead of a neutron star in a large number of cases. Averaging over all spectral types, the number of Be + WD systems should be 7 to 10 times that of Be + neutron stars (see e.g. Raguzova 2001). The discovery or the absence of these low luminosity hard X-ray sources in deep surveys of the Galaxy can bring valuable constraints on the current theories of binary evolution leading to the X-ray bright systems.

With exposure times in the range of 10 to 30 ksec the EPIC cameras of XMM-Newton reach flux limits of $\sim 3 \cdot 10^{-15} \text{ erg cm}^{-2} \text{ s}^{-1}$ in the 0.5 to 2.0 keV soft band and of $\sim 3 \cdot 10^{-14} \text{ erg}$

$\text{cm}^{-2} \text{ s}^{-1}$ in the 2 to 12 keV hard energy range. The present survey can thus be qualified as medium sensitivity in being about 10 times shallower than the Chandra deep galactic plane survey of Ebisawa et al. (2001, 2005) or the Champlane project of Grindlay et al. (2005) but 10 times deeper than the medium ROSAT survey of Morley et al. (2001) or than the faint ASCA galactic plane survey of Sugizaki et al. (2001). Thanks to its large collecting area, XMM-Newton provides good spectra of relatively faint sources. The total area optically studied so far is $\sim 1.8 \text{ deg}^2$ and data for an additional 0.8 deg^2 have already been collected. In comparison, the area surveyed by Morley et al. (2001) was 2.5 deg^2 while those covered by Chandra are of 0.07 deg^2 and 1.1 deg^2 for the Ebisawa et al. (2005) and Grindlay et al. (2005) projects respectively. Champlane aims to eventually cover about 8 deg^2 .

A large part of the optical data presented in this paper were acquired in the framework of the AXIS project (“An XMM-Newton International Survey”¹). AXIS was designed to make the best use of the instruments and telescopes available at the Observatorio de Roque de los Muchachos in the Canary Islands. Other observations were later obtained at the European Southern Observatory (ESO, La Silla Chile and Paranal), at the Canada-France-Hawaii telescope, and at the Observatoire de Haute-Provence (OHP, France).

The paper is organised as follows. We first discuss the characteristics of the selected XMM-Newton fields, the X-ray source extraction, the optical observations and data reduction methods. The next section is devoted to optical identifications. The properties, relative contributions and spatial distributions of the stars, hard galactic sources and background AGN are discussed in the last section.

The data presented in this paper will be distributed through the general interface available at the XMM-Newton SOC. In parallel, the Survey Science Center will also provide a dedicated database allowing advanced browsing of the entire optical and X-ray data set. Identification tables will be available through the Vizier server.

2. XMM-Newton data

2.1. Field selection

Many of the target fields studied in this paper were selected very early after the launch of the satellite. At that time, only a limited number of XMM-Newton observations were available. The specific constraints put on this programme to select fields at low galactic latitude, observable from the northern location of the Canary Islands combined with the avoidance of specific sky areas resulting from the southern orbit of XMM-Newton (mainly the part of the Milky Way located in the Cygnus constellation) yielded a rather limited range of possibilities. Target fields (see Table 1) were selected for their good X-ray quality (depth and low background) and chosen in directions void of large extended diffuse emission or bright sources. We also avoided atypical regions such as known star forming complexes.

¹ see <http://www.ifca.unican.es/xray/AXIS>

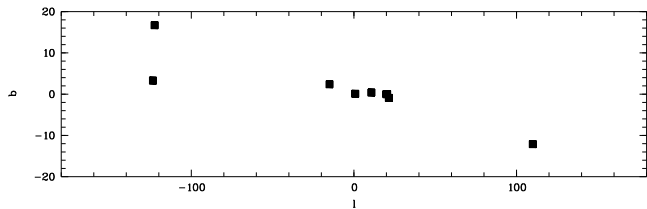


Fig. 1. Distribution of the target fields in galactic longitude and latitude

The earliest available field was that centered on the SNR G21.5-0.9. It consists of several pointings arranged around the central SNR source which was used for the purpose of calibrating the response of the EPIC cameras at various off-axis angles. Since this field was also observed by Chandra for similar calibration purposes, good positions are available for some EPIC sources. The G21.5-0.9, GRB 001025, Ridge 3, Ridge 4 and Z And fields were mostly observed from the Canary Island telescopes in the framework of the AXIS project. The remaining four directions were observed using ESO telescopes. Finally, some of the optically bright candidates in the Z And field were studied at the Observatoire de Haute-Provence.

We show in Fig. 1 the location of the directions investigated in this survey. The distribution in galactic latitude and longitude is far from being homogeneous but is suitable to highlight the main population changes in directions far from and close to the central regions of the Galaxy. Apart from three fields located at $|l| \geq 100^\circ$ and at relatively large galactic latitudes ($|b| = 3^\circ - 16^\circ$), the rest of the observations are concentrated at $|l| \leq 22^\circ$ and $|b| \leq 2.4^\circ$. As stated in the introduction, we are currently investigating more fields in directions suitable to bridge the gaps in galactic longitudes and latitudes. Another field based study currently carried out by the SSC consists in studying with 2-m class telescopes the bright part of the X-ray stellar population in 17 low latitude additional XMM-Newton observations amounting to $\sim 3 \text{ deg}^2$. The results of these studies will be presented in separate papers.

The relatively narrow range of galactic latitudes considered in the galactic fields discussed here does not allow us to fully highlight the expected variation of the density of active coronae with galactic latitude. We therefore built a high galactic latitude “control” sample of stellar X-ray sources from the AXIS programme (Barcons et al. 2002). The high b group consists of 34 stars extracted from 18 XMM-Newton fields ($|b| = 23^\circ - 80^\circ$, average value 50°) in a total survey area of 2.3 deg^2 . The flux limit is $2 \cdot 10^{-14} \text{ erg cm}^{-2} \text{ s}^{-1}$ in the 0.5 to 4.5 keV band, slightly above that used in the galactic plane. This high galactic latitude sample is however restricted in size and depth and a thorough discussion of the variation of stellar density with galactic latitude will require the additional use of larger and deeper samples (Herent et al. 2005).

2.2. Source extraction

In this study, we only consider sources detected in the EPIC pn camera with a detection maximum likelihood larger than 8 in the combined 5 energy bands. This limit ensures that no

more than about one source per field is spurious in a given energy band (User Guide for the original 1 XMM catalogue version 1.0.1). However, EPIC MOS camera data were used to improve source positions or hardness ratio definitions whenever possible. Some of the brightest sources detected on the MOS camera only, because of their location in the EPIC pn CCD gaps or outside EPIC pn field of view, were also considered for optical identification but are not reported here. X-ray source extraction was performed several times in the course of the optical observations in order to benefit from the best available calibrations, both spatially and spectrally. Early SAS versions which could not provide the best positional accuracies were used in the first observing runs starting in June 2000. As far as optical identifications are concerned, the most important improvement is the application of the *eposcorr* task which corrects the residual attitude error by cross correlating EPIC positions with the brightest USNO-A2.0 optical positions in the field. After *eposcorr* correction, the systematic positional error drops from 1.5 to 0.5 arcsec. In rare cases, the *eposcorr* task fails to find the right bore-sight correction. We checked that no such problem occurred in any of our fields. All X-ray sources were visually inspected in order to remove the numerous spurious detections which plagued the first reductions, in particular, the out-of-time events and all sources resulting from erroneous background subtraction or remaining diffuse emission. Such a screening process obviously introduces some human based bias which cannot be described in a straight forward manner. This bias mainly affected the way we prioritized sources scheduled for optical follow-up. Whenever available, the 1 XMM entries (Watson et al. 2003) extracted with SAS version 5.0 (2002-05-22) were used as a basis for the final observation source list. In particular, we use the energy bands of the 1 XMM catalogue and the EPIC pn hardness ratio 2 is defined as $\text{pn_HR2} = [\text{Cts}(2.0-4.5 \text{ keV}) - \text{Cts}(0.5-2.0 \text{ keV})] / \text{Cts}(0.5 - 4.5 \text{ keV})$ where $\text{Cts}(\text{band})$ is the EPIC pn count rate in the given band. The 1 XMM catalogue is human screened and can thus be considered as the cleanest source extraction available at the time we write this paper. We imposed $\text{SUMM_FLAG} > 0$ in order to remove sources flagged as possibly spurious at the screening stage. In order to properly compute likelihood of matches with bright optical objects we used version 1.1 of the 1 XMM catalogue which corrects in a statistical manner the positional errors of many of the faint sources (XMM-Newton news #45). Since the interplay of the intrinsic spectra and interstellar absorption can produce a large range of energy distributions, we retained detections in all energy bands and sorted source lists using count rates integrated over the entire EPIC energy range. No flux limit or maximum off axis distance was applied. This has the consequence that the sensitivity decreases by up to 70% when moving from the center to the edge of the EPIC field. We obviously discarded the target of the observation from our study.

2.3. Notes on individual fields

PKS 0745-19 offset: This field was observed in order to serve as reference background for studying the nearby cluster of

Table 1. Galactic target fields

Field	RA	Dec	l	b	Gal N_{H} cm^{-2}	Epic pn exp (ks)	Observation ID
PKS 0745-19 off	07h48	-19°06′	236.4°	+3.3°	$3.0 \cdot 10^{21}$	36	0105870201
GRB 001025	08h36	-13°04′	237.4°	+16.3°	$4.0 \cdot 10^{20}$	26	0128530301
GRO J1655-40	16h54	-39°52′	345.0°	+2.4°	$7.5 \cdot 10^{21}$	21	0112460201
GC 2	17h45	-28°10′	0.8°	+0.1°	$3.4\text{-}7.5 \cdot 10^{23}$	13	0112970201
WR 110	18h07	-19°23′	10.8°	+0.4°	$5.5 \cdot 10^{22}$	23	0024940201
Ridge 3	18h27	-11°29′	20.3°	+0.0°	$1.1 \cdot 10^{23}$	8	0104460301
Ridge 4	18h28	-11°07′	20.3°	+0.0°	$1.1 \cdot 10^{23}$	5	0104460401
G21.5-0.9 (rev 60)	18h33	-10°34′	21.5°	-0.9°	$9.0 \cdot 10^{22}$	20	0122700101
G21.5-0.9 (rev 62)	18h33	-10°36′	21.4°	-0.7°	$9.0 \cdot 10^{22}$	25	0122700301
Z And	23h33	+48°49′	110.0°	-12.1°	$1.5 \cdot 10^{21}$	17	0093552701

galaxies PKS 0745-19. This is a low background, deep exposure and rich field. **GC 2:** This pointing is part of a small survey of the central regions ($\sim 2^\circ$) of the Galaxy. GC2 is the field displaying the least diffuse emission and is void of bright sources. Another advantage of this field is a total absorption lower than in the exact direction of the galactic center which in principle favours the detection at optical wavelengths of more counterparts of remote X-ray sources. **GRO J1655-40:** This field is not part of the 1 XMM catalogue. We reprocessed the observation in June 2003 with the then latest version of the SSC pipeline by mid 2003 (02000050/20021220.132037). About ten of the 61 XMM-Newton sources are also present in the Chandra observation 400012 obtained in July 2000 with the ACIS-I camera. We did not find clear systematic deviations of the *eposcorr* corrected XMM-Newton positions with respect to the Chandra positions and therefore no attempt was made to use these to correct the EPIC coordinates. Chandra positions were of course considered to guide the optical identification of these ten sources. The maximum likelihoods of detection in each of the EPIC pn band were corrected to their true value following the recommendations given in XMM-News # 29. Finally, the original errors on positions were multiplied by 1.66 in order to correct for the underestimation of the positional errors arising in the used version of the source detection chain on faint X-ray sources. **GRB 001025:** This target of opportunity (TOO) pointing has the highest galactic latitude in our sample. This field is also the one with the lowest spectroscopic identification rate as a result of the relatively small observing time left within the AXIS programme at the time this field was started. **G21.5-0.9:** A total of 7 XMM-Newton pointings were available at the time we completed the optical identification work. A dedicated reprocessing was done in 2002 for two of the deepest pointings (in revolutions 60 and 62) for which the best wide-field imaging was available. The presence of intense extended emission from the SNR yielded many false source detections which were efficiently removed by human screening. In this paper we report only on optical identifications in these particular two fields with a total area of 0.27 deg^2 . Unfortunately, 1 XMM catalogue data are only available for one of the two observations (that obtained during revolution 62). For this observation the *eposcorr* task was able to correct EPIC positions using a number of optical matches yielding a mean 90% confidence radius of $3.2''$.

Chandra repeatedly observed this field for calibration purposes and we used these positions to validate some of the possible optical identifications. The histogram of the distance between Chandra and XMM-Newton positions peaks at $3''$ and sharply drops at $\sim 5''$. **Z And:** XMM-Newton observed this field twice. We used as reference the deepest and cleanest observation (obsid = 0093552701) in which a total of 40 sources are detected.

2.4. Correction for completeness

Because of vignetting, the sensitivity of the EPIC pn camera severely drops by $\sim 70\%$ at large off axis angles, the exact value depending on energy. The area lost in bad pixels and inter CCD gaps must also be properly taken into account. We first tried to use SAS created sensitivity maps to correct the $\log N(>S)\text{-}\log S$ curves for the reduced area sampled at faint flux. However, in SAS version 6.0 and earlier, the sensitivity maps made by the *esensmap* task were not realistic enough to provide a reasonably accurate correction. Instead we used the results of the 1 XMM catalogue reprocessing to derive an empirical relation between the smallest total number of counts PN_{tot}^i , detected above a given maximum likelihood as a function of the local background ($\text{PN}_{\text{i,BG}}$ in units of counts per pixels) where i is the standard energy band definition used in the 1 XMM catalogue. The total number of count PN_{tot}^i was computed as the product of the source count rate (PN_{i} corrected at optical axis) times the exposure time ($\text{PN}_{\text{i,EXP}}$, which takes into account the vignetting). We checked that the lower envelope of this relation did not depend much on the off-axis angle, i.e. that the extended shape of the PSF near the edge of the field of view had no strong influence on the detection limit. A parabolic curve was fitted by eye to the lower envelope of the $\text{PN}_{\text{tot}}^i / \text{PN}_{\text{i,BG}}$ distribution for $\text{PN}_{\text{i,DET_ML}} \geq 8$ in the 0.5-2 keV, 2.0-4.5 keV, 4.5-7.5 keV, 7.5-12.0 keV and 0.5-4.5 keV bands. For each source, the camera area sensitive enough to allow its detection was estimated from the local source background and from the observation exposure map. This procedure, albeit empirical yielded a satisfactory correction for completeness.

3. Optical data

3.1. Imaging

Wide-field imaging data were obtained with the Isaac Newton Telescope (INT), with the Canada France Hawaii Telescope (CFHT) and with the ESO-MPG 2.2m telescope. A first description of the INT data can be found in Yuan et al. (2003). All cameras covered in a single image the entire 30' diameter field of view of the XMM-Newton EPIC cameras. At the 2.5m INT we used the Wide-Field Camera in dark time and obtained relatively deep imaging through the g' , r' , i' , z and $H\alpha$ bands. At the CFHT, narrow filter $H\alpha$ ($\lambda_c = 6584\text{\AA}$, FWHM = 76\AA) and $H\alpha$ continuum ($\lambda_c = 6453\text{\AA}$, FWHM = 90\AA) imaging was obtained with the CFH12K camera in addition to some broad band i and r images. Finally, the B, V, R, I, z and $H\alpha$ filters were used at the ESO 2.2m telescope with the Wide Field Imager. Tables 2, 3 and 4 list imaging exposure times in the various filters used.

Images were reduced using standard methods to correct for bias, non-linearity, flat field and fringing. The WFC pipeline procedures are described in the Cambridge Astronomy Survey Unit web pages (<http://www.ast.cam.ac.uk/~mike/casu/>). Astrometric calibration was performed in the two different ways described in Barcons et al. (2002) resulting in a final accuracy better than 0.3 to 0.5". At the CFHT we re-sampled the individual images using the Terapix software, reaching a final astrometric accuracy of about 0.15". WFC data were first reduced using the *msred* package and then fed into the Terapix software to reach a similar astrometric accuracy as at the CFHT. In all cases, photometric zero points were derived from observations of photometric standards during the same night and standard colour transformations were applied. As a check, the R band photometry was compared with GSC 2.2 photographic R magnitudes and found to be correct. Corresponding observing runs took place in the time interval 2000-2003.

Table 2. Wide-Field imaging at the INT. Exposure times in seconds

Field	g	r	i	z	$H\alpha$
GRB 001025	600	900	1200	1200	2400
WR 110	600	600	1200	1200	-
Ridge 3	600	600	-	1200	2400
Ridge 4	600	600	1200	1200	-
G21.5-0.9	1200	600	1200	600	6000
Z And	600	600	1200	1200	-

Because of the rather long exposure time, many of the relatively bright optical counterparts of the stellar X-ray sources were actually saturated. For these objects we use the GSC 2.2 magnitudes as a first choice and USNO-A2.0 as a second possibility. A distinct imaging program aiming at the photometric calibration of the optically bright end of the stellar population of the northern fields was performed at the OHP and is currently being analysed. The results of this project will be presented in a subsequent paper.

Table 3. Wide-Field imaging at ESO-La Silla (WFI on the ESO-MPG 2.2m). Exposure times in seconds

Field	B	V	R	I	z	$H\alpha$
PKS 0745-19 off	180	4980	180	120	120	6300
GRB 001025	200	5880	200	200	-	-
Ridge 3	-	9630	-	2400	-	-
Ridge 4	-	8100	-	-	-	-
G21.5-0.9	900	900	600	1200	300	-
G21.5-0.9 off1	1000	300	600	1200	300	-
G21.5-0.9 off2	1800	2100	600	1200	300	-
G21.5-0.9 off3	-	300	600	1200	300	-
G21.5-0.9 off4	-	300	600	1200	300	-

Table 4. Wide-Field imaging at the CFHT. Exposure times in seconds

Field	R	I	$H\alpha$	$H\alpha$ continuum
WR110	400	400	3480	3480

3.2. Spectroscopy

Spectroscopic observations were carried out in three distinct observatories using five different spectrographs. The first spectra were obtained with the AUTOFIB2/WYFFOS multi-fibre spectrograph mounted on the 4.2m William Herschel Telescope (WHT) at the Observatorio del Roque de Los Muchachos. The space density of the EPIC sources in the galactic plane is about 100 deg^{-2} and thus suitable for observations with the WYFFOS multi-fibre instrument. Because of low galactic latitude and of the rather large error circles resulting from the first source extractions used in 2000, up to 3 optical candidates at magnitudes brighter than $R \sim 19-20$ (the limiting magnitude of the multi-fibre instrument) could be found in the EPIC error circle. Each field was thus observed 3 times with fibre positions slightly displaced in order to cover all candidates. The high sky background resulting from the large fibre diameter of 2.7" did not allow us to reach the best sensitivity achievable with multi-fibre instruments. A large fraction of the identifications had thus to be done with long slit spectroscopy. ISIS was used at WHT during several observing runs in 2000 and 2001. Details on the instrument setup and observing procedure can be found in Barcons et al. (2002). At ESO La Silla we used the 3.6m telescope and the EFOSC2 focal reducer on three occasions, July 9-12 2002, February 28 - March 5 2003 and June 27 - July 3 2003. Additional spectra of the faintest candidates were obtained with the ESO-VLT UT4 with FORS 2 in July 2003. Finally, some relatively bright optical counterparts in the field of Z And were observed from OHP with the CARELEC spectrograph and the 1.93 m telescope. Table 5 shows the details of the instrumental setups relevant to this work.

All CCD frames obtained at ESO and OHP were corrected for bias and flat-fielded using standard MIDAS procedures. Arc lamp exposures of various atomic species were used to derive a wavelength calibration generally accurate to better than 5% of the spectral resolution. One dimensional spectra were extracted with a procedure optimizing the accumulation region in order to reach the best signal to noise and using sky back-

Table 5. Spectroscopic settings

Telescope	Instrument	Spectral range	Spectral resolution (Å)	Slit width (")	Comments
WHT	WYFFOS	3900-7100	6-7	2.7	Fibers
WHT	ISIS	3500-8500	3.0-3.3	1.2 - 2.0	
ESO-3.6m	EFOSC2	3185-10940	59	1.5	Grism #1
ESO 3.6m	EFOSC2	3860-8070	17.3	1.5	Grism #6
ESO 3.6m	EFOSC2	3095-5085	7.1	1.5	Grism #14
ESO-UT4	FORS2	3850-7500	15	1.0	GRIS_300V
OHP-1.9m	CARELEC	3760-6844	5-7	1.0-2.0	133Å/mm

ground cleaned from cosmic-ray impacts. All spectra were corrected for atmospheric extinction and calibrated in flux using spectrophotometric standards. The requirement to put two optical candidates in the slit prevented it being orientated along or close to the parallactic angle. Consequently, the accuracy of the flux calibration, while generally good at least to derive relative fluxes, may still suffer from moderate spectral distortion in some instances.

Spectral classification can be difficult at the low spectral resolution and signal to noise ratio resulting from the faintness of many stellar counterparts. In order to be the most unbiased we designed a MIDAS procedure in which flux calibrated reference spectra degraded to the spectral resolution of the observation are fitted to the observed spectrum by adjusting mean flux and interstellar absorption. We used standard spectra from the NASA/JPL NStars project and from Jacoby et al. (1984). We checked that the best fit $E(B-V)$ was in general consistent with that derived from the photometry. However, remaining spectral distortions caused by atmospheric refraction introduce some scatter in the relation. The spectral fitting process was visually controlled and checked by monitoring the behaviour of several important diagnostic lines (Turnschek et al. 1985; Jasheck & Jasheck 1987). We estimate that spectral classification is accurate to one subclass.

4. Optical identifications

4.1. Identification Strategy

Optical crowding makes the identification of XMM-Newton sources in the galactic plane difficult. The SAS task *eposcorr* corrects EPIC positions for residual attitude errors by matching the positions of XMM-Newton sources with entries in the USNO-A2.0 catalogue. When applicable, i.e, if the field stellar density is not too high to confuse cross matching, this process can significantly reduce the 90% confidence error circle by diminishing the assumed systematic errors and thus considerably ease optical identification. Typically, raw positions have 90% confidence error radii of the order of 4-5" while attitude corrected positions have 90% confidence error radii of the order of 3".

In a large number of cases, the XMM-Newton error circle contains a relatively bright optical object. This is consistent with the fact known from previous ROSAT surveys that the majority of soft galactic X-ray sources are active stars. There is obviously a limiting magnitude at which the appearance of a

relatively bright optical object in the EPIC error circle has a high probability to be a chance coincidence. We estimated this magnitude by accumulating $\log N(>S)$ - $\log S$ curves for all optical objects detected in the EPIC field of view using either our wide-field imaging data or USNO-A2.0,-B1.0 or GSC 2.2 extractions. The interplay of intrinsic stellar colours, interstellar reddening and detector sensitivity yields best sensitivity in the R band.

We list in Table 6 the outcome of the *eposcorr* task for the different fields considered in this study together with the mean values of the 90% confidence error radius extracted from the corrected 1.1 version of the 1 XMM catalogue. The table also shows the R magnitudes for which the probability that the presence of an optical object in the small EPIC error circle is due to a chance coincidence is 5% and 1%.

Table 6. Mean 90% confidence radii (for all sources with total detection maximum likelihood larger than 8) and faintest R magnitude for identification by positional coincidence given at the 5% and 1% contamination level

Field	<i>eposcorr</i> applied	$\langle r_{90} \rangle$ (arcsec)	R_{lim} (5%)	R_{lim} (1%)
PKS 0745-19 off	yes	2.70	19.19	15.64
GRB 001025	yes	2.88	> 20.00	> 18.5
GRO J1655-40	yes	4.64	18.79	15.30
GC 2	yes	3.05	17.58	14.94
WR 110	yes	3.14	16.70	14.74
Ridge 3	yes	3.09	17.20	15.00
Ridge 4	no	4.41	16.66	14.86
G21.5-0.9	yes	3.16	18.09	15.94
Z And	yes	3.04	19.31	16.45

At low galactic latitudes, we identified an X-ray source as an active stellar corona when its probability to fall by chance in the 90% confidence error circle was at most 5%. In most cases we could obtain optical spectroscopy of these candidates from which a spectral type could be derived. We also obtained spectra of fainter candidates, looking for companion Me stars for instance. In a few cases we rejected the bright star as a possible counterpart on the basis of an extremely high interstellar absorption incompatible with the soft X-ray spectrum. Unfortunately, the relatively faint flux of the stars in the near UV together with the low spectral resolution used and still strong photospheric continuum do not allow the detection of

Ca H&K or Balmer emission lines in the vast majority of the counterparts. This situation differs from that of the ROSAT all-sky survey (Motch et al. 1997a) where the shorter distances and consequent lower interstellar absorption of the X-ray emitting active coronae allowed clear detection and measurement of the chromospheric Ca H&K diagnostic emission lines.

This 5% level was chosen as the best compromise between the need not to lose too many genuine counterparts by restricting too much the size of the XMM-Newton error circle and the requirement to keep as low as possible the number of random matches with bright optical objects. With a typical number of ~ 60 sources per field, we miss 6 optical counterparts, among which about 3 will be stellar coronae on average (see below). A 5% level of contamination implies that the same amount of 3 X-ray sources will be unduly identified with bright optical objects.

However, in many cases the error circle is void of bright objects, and we have to collect optical spectra of typically 3-4 candidates brighter than $R \sim 22$ before possibly finding a reliable identification. For soft sources, we observed faint red objects, Me star candidates, with the highest priority. At the sensitivity of our survey, stellar counterparts fainter than $R \sim 16 - 17$ are mostly late K-M stars. Balmer emission is found in all active M stars and in a fraction of the most active K stars. Cataclysmic variables and Be/X-ray binaries are also $H\alpha$ emitters. Our narrow band $H\alpha$ and $H\alpha$ continuum imaging together with broad band colour information was thus used to prioritize efficiently optical candidates for spectroscopy (Herent et al. 2003).

For the fields located at very low galactic latitudes, we put a low priority on the optical identification of sources with hardness ratios consistent with those expected from absorbed AGN and with only faint optical candidates in the error circle (typically one third of the sources). Below 4.5 keV, the typical background AGN spectrum was assumed to be a power-law with a photon index $\Gamma = 1.9$ as observed in BLAGN detected in the XMM-Newton serendipitous surveys of similar flux range as here (Mateos et al. 2005). At higher energy we used a photon index of 1.4 in order to match that used in Campana et al. (2001). This selection is very efficient in directions of high absorption and still leaves a large range of possible N_{H} (or intrinsic spectral hardness) for galactic objects.

The total galactic absorption was estimated by two independent means. We used first the extinction derived from far infrared emission from Schlegel et al. (1998). In addition we used the HI map of Dickey and Lockman (1990) and the high resolution CO map of Dame et al. (2001). The total N_{H} was then computed as $N_{\text{H1}} + 2 \times N_{\text{H2}}$ with $N_{\text{H2}} = 2.7 \cdot 10^{20} \times T_{\text{co}}$.

4.2. Identification statistics

We list in Table 7 the statistics of optical identifications in each field and for the entire galactic sample. The limiting magnitude defined here as the faintest estimated magnitude at which we can detect emission lines typical for a CV or a Me star depends on the instrumental setting. Our sample contains a total of 411 EPIC pn sources. The vast majority of the optical identifications are with active coronae. Because of the relatively high

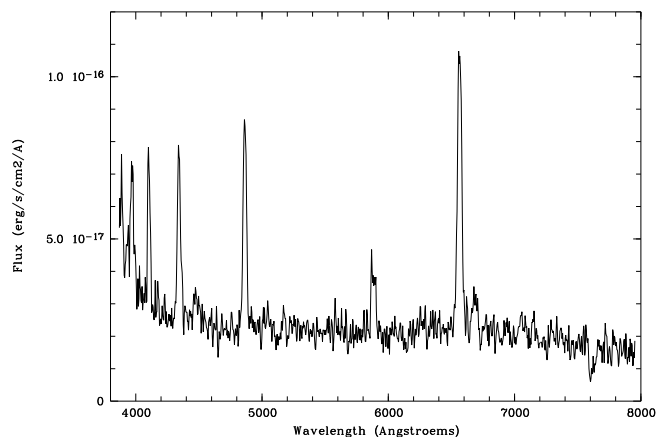


Fig. 2. Optical spectrum of the cataclysmic variable 1 XMMJ074743.5-185654

galactic latitude and correspondingly low N_{H} it was still possible to spectroscopically identify AGN in the PKS 0745-19 offset, GRB 001025 and Z And fields. At lower latitudes, galactic absorption becomes too large for our instrumentation to detect extragalactic sources. The only low b extragalactic source is in the field of G21.5-0.9 (XMMU J183225.4-103645, Nevalainen et al. 2001) and was identified as an X-ray bright cluster of galaxies, seen through over 50 magnitudes of absorption in the visual, on the basis of X-ray source extent, energy distribution and redshifted iron line. Identified accreting sources or candidate accreting sources only represent $\sim 1\%$ of the total. Unfortunately, the overall fraction of unidentified sources remains high ($\sim 60\%$ for the entire sample). We note, however, that the identification rate rises to $\sim 50\%$ in the low galactic latitude fields with the deepest spectroscopic limiting magnitude. It is clear that our instrumental setting, both in terms of sensitivity and wavelength used does not allow us to detect the optical counterparts of most of the extragalactic sources, especially in the low latitude fields. Background AGN may still account for a large fraction of the X-ray sources, in particular the hardest ones, even at very low galactic latitudes. Our instrumental setting also seems not efficient enough to unveil most of the relatively remote population of low-mass accreting sources in the deep galactic plane. Infrared spectroscopy would certainly allow us to identify some of them. Another limitation intrinsic to XMM-Newton comes from the relatively large error radii (typically $3''$). In the densest regions of the Galaxy, a large number of faint optical or near infrared candidate stars can be found within the error circles requiring tedious and long spectroscopic observations for each of them.

4.3. Accreting candidates

4.3.1. Cataclysmic variables

The only cataclysmic variable identified in this work was found in the field of PKS 0745-19 offset (source # 4). The counterpart is relatively bright ($R \sim 20.78 \pm 0.03$). Its optical spectrum lacks the He II $\lambda 4686$ line often found in polars and intermediate polars (see Fig. 2) The equivalent width of the

Table 7. Optical identifications

Field	l	b	Gal N_H	Rlim Spect	N tot	Active Coranae	Accreting Candidates	Extra Galactic	Unidentified
PKS 0745-19 off	236.4°	+3.3°	3.0 10^{21}	21	71	21 (29.6%)	1 (1.4%)	17 (24.0%)	32 (45.0%)
GRB 001025	237.4°	+16.3°	4.0 10^{20}	19	72	5 (6.9%)	0	8 (11.1%)	59 (82.0%)
GRO J1655-40	345.0°	+2.4°	7.5 10^{21}	19	61	24 (39.3%)	0	2 (3.3%)	35 (57.4%)
GC 2	0.8°	+0.1°	3.4-7.5 10^{23}	19	40	20 (50.0%)	0	0	20 (50.0%)
WR 110	10.8°	+0.4°	5.5 10^{22}	21	61	24 (39.3%)	1 (1.6%)	0	36 (59.1%)
Ridge 3	20.3°	+0.0°	1.1 10^{23}	21	19	12 (63.2%)	0	0	7 (36.8%)
Ridge 4	20.3°	+0.0°	1.1 10^{23}	19	12	3 (25.0%)	0	0	9 (75.0%)
G21.5-0.9	21.5°	-0.8°	9.0 10^{22}	19	35	10 (28.6%)	2 (5.7%)	1 (2.9%)	22 (62.8%)
Z And	110.0°	-12.1°	1.5 10^{21}	19	40	11 (27.5%)	0	1 (2.5%)	28 (70.0%)
Total					411	130 (31.6%)	4 (1.0%)	29 (7.1%)	248 (60.3%)

$H\alpha$ line is large, $\sim 140 \text{ \AA}$. Both a thin thermal Raymond-Smith model with $kT \sim 3.6 \text{ keV}$ or a power-law spectrum with $\Gamma \sim 2.5$ provide good representations of the observed EPIC pn energy distribution and implies a 0.2-12 keV X-ray flux of $\sim 1.6 \cdot 10^{-13} \text{ erg cm}^{-2} \text{ s}^{-1}$. In both models, the interstellar absorption is small ($N_H \leq 4 \cdot 10^{21} \text{ cm}^{-2}$). Both the Kolmogorov-Smirnov test ($KS = 4.7 \cdot 10^{-2}$) and the χ^2 test ($\chi^2 \sim 10^{-19}$) suggest that the source is variable. The comparatively soft X-ray temperature and the optical spectrum suggest a dwarf nova nature.

4.3.2. Massive X-ray binary candidates

In three cases, we detect X-ray emission from a Be star at a level which is significantly above that expected for ‘normal’ early type stars (Cassinelli et al. 1994). In addition to the case of SS 397 already mentioned in Motch (2000), we also find excess X-ray emission from USNO 0750-13549725/WL 9 which is the brightest star in the open cluster NGC 6649. Both sources were incidentally found in the field of G21.5-0.9. The third candidate is a faint and very absorbed $H\alpha$ emitting star discovered in the field of WR 110.

SS 397: optical spectroscopy indicates a B0.5Ve star with an $H\alpha$ EW of -33 \AA (see Fig. 3). Dedicated imaging observations at the INT in 2001 yield the following magnitudes: $V=12.454 \pm 0.008$, $B-V = 1.372 \pm 0.011$, $V-R = 0.982 \pm 0.011$. The interstellar $E(B-V)$ is somewhat uncertain since the star is probably intrinsically reddened by the contribution of a large circumstellar disc. Taking into account possible errors on the absolute magnitude, we estimate that the distance to SS 397 is in the range of 1.4 to 3.0 kpc. The source was detected in 3 different XMM-Newton observations (0112700101, 0112700201 and 0112700301). Its X-ray spectrum is hard and can be fitted by a thin thermal ($kT \sim 12 \text{ keV}$) or a power law + Gaussian line at 6.4 keV ($\Gamma \sim 1.7$) as well. For both models, the 0.2 - 12 keV flux corrected for absorption varies by less than 20% between observations with a mean value of $7 \cdot 10^{-13} \text{ erg cm}^{-2} \text{ s}^{-1}$, corresponding to X-ray luminosities in the range of 1.6 to $7.5 \cdot 10^{32} \text{ erg/s}$.

USNO 0750-13549725/WL 9 in NGC 6649: The counterpart of the X-ray source is the brightest star in NGC 6649 and is located close to its center. CCD photometry was obtained

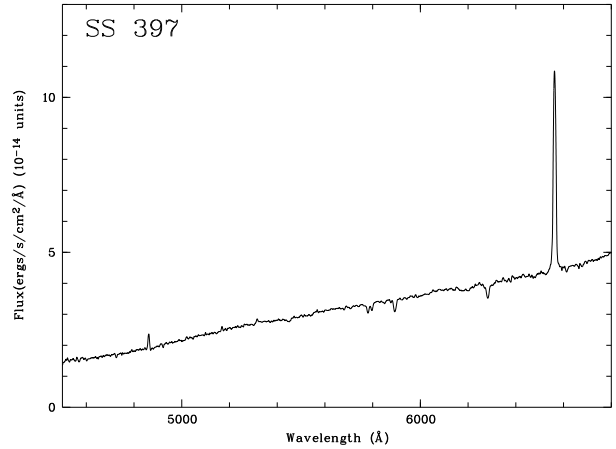


Fig. 3. Optical spectrum of the Be/X-ray candidate SS 397 obtained at the WHT with the ISIS instrument

from Walker & Laney (1987); $V = 11.73$, $B-V = 1.28$, $U-B = 0.06$. We find a B1-1.5 IIIe spectral type with an $H\alpha$ equivalent width of -36 \AA and a double peaked profile (see Fig. 4). The distance to the cluster is 1.6 kpc with a mean $E(B-V)$ of 1.38 (Turner 1981). Two XMM-Newton observations (0112700101 and 0112700401) cover the location of the source. The X-ray spectrum is as hard as that of SS 397 with thin thermal temperatures of the order of 10 keV or a power law photon index of ~ 1.4 . Again, we see little variations between the two observations with a mean 0.2-12 keV X-ray flux corrected for absorption of $1.1 \cdot 10^{-12} \text{ erg cm}^{-2} \text{ s}^{-1}$ corresponding to an X-ray luminosity of $3.3 \cdot 10^{32} \text{ erg s}^{-1}$. Interestingly, Marco et al. (2006) show that the star is a blue straggler and is thus likely the result of massive binary evolution, although this is no real proof that a compact remnant orbits around the star.

The faintest Be/X-ray candidate was found in the field of WR 110 (source # 33, see accompanying tables). We detect $H\alpha$ emission with an equivalent width of $\sim 50 \text{ \AA}$ from a faint red star ($R = 22.0$, $R-I=2.6$). The absence of TiO features excludes a Me star nature and the R-I colour index indicates high interstellar absorption (see Fig. 5). If the counterpart is an intrinsically blue object then A_V is of the order of 12.5 or $N_H = 2.2 \cdot 10^{22} \text{ cm}^{-2}$, i.e. about half of the total expected galactic absorption in that direction. The high interstellar reddening and ac-

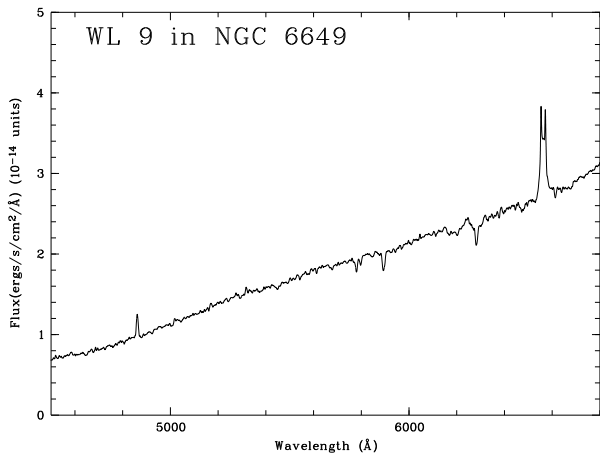


Fig. 4. Optical spectrum of the Be/X-ray candidate WL 9 in NGC 6649 obtained at the WHT with the ISIS instrument

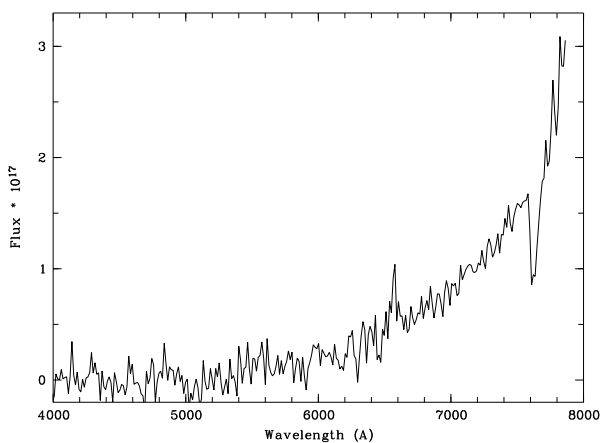


Fig. 5. Optical spectrum of a faint accreting Be star candidate in the field of WR 110

cordingly large distance and optical luminosity rules out a CV nature. A Be star identification thus seems likely. At a distance of ~ 12 kpc the X-ray luminosity is of the order of $1.3 \cdot 10^{33}$ erg s^{-1} (0.5 - 7.5 keV). The source is hard ($pn_HR2 = 0.07 \pm 0.18$) roughly consistent with a relatively hard powerlaw seen through the absorption detected in the optical. Unfortunately the source is not bright enough to allow a more detailed spectral analysis.

SS 397 and USNO 0750-13549725/WL 9 exhibit X-ray spectra much harder than those emitted by 'normal' OB stars ($kT \sim 0.5$ keV see e.g. Cassinelli et al. 1994). Even their soft (0.5-2.0 keV) X-ray luminosity lies slightly above that radiated by normal OB stars of the same spectral type (Berghöfer et al. 1997). XMM-Newton observations of two low X-ray luminosity Be/X-ray candidates discovered in the ROSAT all-sky survey (Motch et al. 1997b), SAO 49725 and HD 161103, reveal a strikingly similar pattern of optical and X-rays features (Lopes de Oliveira et al. 2005). HD 110432 (Torrejon & Orr 2001) might be another similar object. There is now strong evidence that these X-ray emitting Be stars are newly discovered twins of the so far unique γ -Cas star (Motch et al. 2006).

The presence of a strong iron $K\alpha$ 6.4 keV line in all γ -Cas analogs bright enough suggests that the X-ray source resides in the relatively dense regions of the circumstellar disc. Alternatively, the iron line could be due to reflection from the white dwarf surface and/or accretion disc as in cataclysmic variables. In comparison low X-ray luminosity 'classical' Be/X-ray systems such as X Per ($L_X \sim 10^{34}$ erg/s) do not exhibit any iron line indicating a low density environment. A large orbit or an efficiently truncated circumstellar disc can account for this low density. The modest X-ray luminosities radiated by γ -Cas analogs can thus be explained by accretion onto a gravitational well smaller than that of a neutron star, a white dwarf or a neutron star in the propeller mode (see eg Kubo et al. 1998 and references therein). Theories of massive binary evolution do predict the formation of a large number of Be + white dwarf systems (see Raguzova 2001 and references therein) with primaries up to the B0 spectral type. The group of hard and low X-ray emitting Be stars discovered in the ROSAT all-sky survey and now in the XMM-Newton survey could thus be the long sought massive stars + white dwarf binaries.

However, some optical and X-ray features observed in γ -Cas and HD 110432 seem better explained in terms of magnetic star - disc activity and reconnection (see Robinson et al. 2002). In this scenario, however, the reason why some B0 stars are prone to emit hard X-rays and other not is not yet clear.

A detailed X-ray study of SS 397 and USNO 0750-13549725, together with other candidates found in the XMM-Newton GPS survey will be presented in a forthcoming paper.

4.4. Active coronae

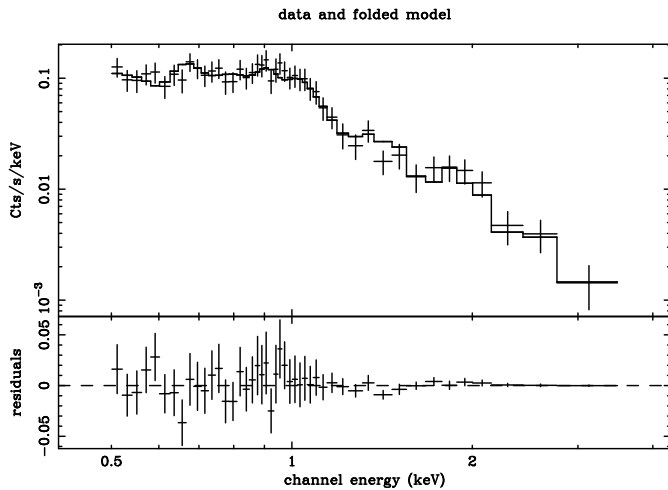
At very low galactic latitudes, the fraction of sources identified with active coronae varies with pointing directions. Whereas in the GRO J1655-40, GC 2 and WR 110 fields, stellar coronae account for 40% to 50% of the X-ray sources, the fraction is only 29% in the field of G21.5-0.9. At the galactic latitude of 3.3° , the rate of identification decreases to $\sim 30\%$.

Spectral types, distances, reddening and luminosities were derived for most stellar identifications in the fields presented here as well as other fields selected solely for the purpose of studying the optically bright X-ray emitting stellar population. Preliminary results and a comparison with the predictions of the stellar population model are presented in Herent et al. (2005). In this first paper, we will concentrate on the analysis of the $\log N(>S)$ - $\log S$ curves and the constraints they can put on the distribution of active stars in the Galaxy.

In the WR 110 and Ridge 3 fields, ($b \sim 0^\circ$), the mean B-V excess of X-ray active stars is about 0.6 (or $N_H \sim 3.5 \cdot 10^{21}$ cm $^{-2}$). We detect active coronae up to 500 pc in the Ridge 3 and 1 kpc in the WR 110 field respectively. Table 8 shows the distribution in spectral types of the stars identified with X-ray sources. At the flux level considered here ($\sim 4 \cdot 10^{-15}$ erg cm $^{-2}$ s $^{-1}$ in the 0.5 to 2.0 keV band), the low $|b|$ active star population displays a distribution in spectral types which is not statistically different from that seen at high $|b|$. The low latitude ROSAT survey (Motch et al. 1997a) also exhibits a similar spectral type distribution in spite of a factor 25 lower sensitivity. The dis-

Table 8. Spectral types of X-ray active stars

Field	A	F	G	K	M
PKS 0745 Off	1	3	11	4	3
GRO J1655-40	1	4	2	6	1
GC 2	0	3	4	3	4
WR 110	2	3	4	10	5
Ridge 3	2	2	3	1	4
G21.5-0.9	0	0	3	3	4
Z And	0	0	3	6	2
Total	6	15	30	33	23
Fraction (%)	5.6	14.0	28.0	30.8	21.5
	± 2.4	± 3.6	± 4.6	± 4.8	± 4.2

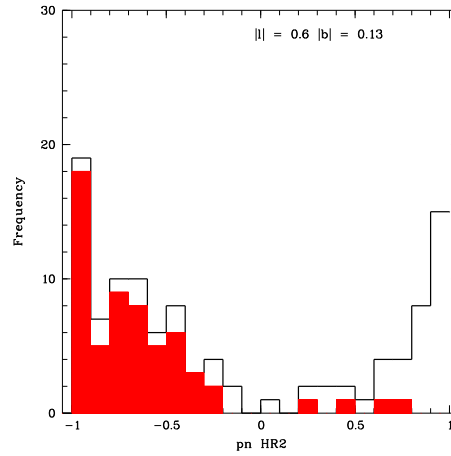
**Fig. 6.** The EPIC pn spectrum of the brightest active corona identified in Ridge 4. Two thin thermal components of $kT = 0.5$ keV and $kT = 1.0$ keV are needed to provide a good fit.

covery of luminous X-ray emission from some A stars is not surprising. Since early A stars lack the convective layer needed to drive a stellar dynamo, generate a magnetic field and a hot X-ray emitting corona, the usual interpretation is that X-rays are emitted by an unseen companion of lower mass. This hypothesis has received support from high spatial resolution optical and X-ray observations, although the possibility remains that some early A and late B stars are intrinsic X-ray emitters (Stelzer et al. 2003).

We show in Fig. 6 the X-ray spectrum of the brightest active corona detected in our sample of star. The source 1 XMM J182845.7-111712 is located in the Ridge 4 field and is identified with a $R = 11.7$ star on the basis of the coincidence in position. We do not have optical spectra for this particular object. Two thin thermal components with $kT = 0.5$ keV and $kT = 1.0$ keV are needed to obtain a good fit to the EPIC pn spectrum. These temperatures are well within the range of those expected for field active stars (see e.g. Schmitt et al. 1990, Guillout et al. 2006a).

5. Additional fields

In order to better constrain the variability of the various galactic components with galactic longitude we extracted from the XMM-Newton archive two groups of fields located at $l = -$

**Fig. 7.** Distribution in pn_HR2 of sources in the “GC series” fields having an error of less than 0.2 on the hardness ratio. Thick black line: all sources. Red histogram: sources with a high probability to have a stellar identification ($LR \geq 5$).

50° (the “Galactic Plane” series) and close to the galactic center (the “GC” series) which includes one of the field already discussed, GC 2. XMM-Newton has repeatedly observed the galactic center area, focusing on Sgr A* and on the very faint transients located within $\sim 1^\circ$ of the galactic center (Wijnands et al. 2005). Table 9 lists the main characteristics of the additional fields used in this study. Source lists were extracted from the 1 XMM catalogue and are therefore in principle free of many spurious detections if one imposes a maximum likelihood larger than 8 and a sum flag greater than 0. All fields were visually examined and checked for the presence of a high particle background and intense diffuse emission. We used the same procedure as for the survey fields to correct $\log N(>S)$ - $\log S$ curves for incompleteness. Since apart from GC 2, we do not have spectroscopic optical identifications we used the likelihood of the matching of an X-ray source with a relatively bright optical object to identify in a statistical manner the foreground stellar component. For that purpose, we used the cross-correlations provided by the XCAT-DB (Michel et al. 2004) with the USNO-A2.0 catalogue. The background density of sources was extracted from Vizier (Ochsenbein et al. 2000) for each individual field and optical $\log N(>S)$ - $\log S$ curves accumulated. We computed the probability that the optical object is at the same position as the X-ray source taking into account statistical and systematic astrometric errors on both the XMM-Newton positions and on the catalogue objects. The probability that an optical object as bright as the one selected is found at that distance was estimated using the optical $\log N(>S)$ - $\log S$ curves. Using the likelihood ratio statistics (de Ruiter et al. 1977) we computed reliability and completeness estimates. Imposing a LR ratio larger than 5 and 3.5 for the “GC series” and “Galactic Plane” fields respectively, ensures that no more than 5% of the cross-matches will be spurious, while keeping a completeness of $\sim 80\%$. The distribution in hardness ratio of the sources with likely stellar identifications (see Fig. 7) is significantly softer than on average and thus validates the statistical identification process.

Table 9. List of XMM-Newton fields entered in the “GC” and “Galactic Plane” series

Obs id	Name	l	b	exp (s)
0112970201	GC2	0.80	+0.07	20319
0112970401	GC4	0.33	+0.03	25319
0112970801	GC8	359.28	-0.03	23751
0112971001	GC10	359.89	-0.35	18572
0112971501	GC3	0.56	-0.03	22270
0112971901	GRO J1744-28	0.02	+0.31	10307
0007420701	Gal. Plane 07	310.86	-0.33	9700
0007420801	Gal. Plane 08	310.83	+0.02	12000
0007421001	Gal. Plane 10	310.83	+0.86	13000
0007425001	Gal. Plane 18	311.45	+0.44	7500

6. Discussion

6.1. X-ray stellar population models

The Einstein and ROSAT satellites have demonstrated that stellar X-ray emission is widespread over the entire HR diagram (Vaiana et al. 1981, Guillout et al. 1999). There is however a dividing line between the solar type stars (F-M type stars), where X-ray emission results from magnetic heating of the corona and the early type stars (earlier than about B5) in which shocks in the high velocity wind are the main source of X-rays. In solar type stars, X-ray emission clearly relates to the presence of a convection layer in differential rotation which is responsible for the generation of the magnetic field through the dynamo process. As rotation slows down with age, stellar activity decreases. Rotation plays indeed a major role since old close binaries which are tidally locked with orbital rotation can be strong X-ray emitters (e.g. V 471 Tau, Wheatley 1998). X-ray observations of nearby open clusters have indeed revealed a strong dependency of the X-ray luminosity with age, the mean X-ray emission decreasing by a factor of 10 in 1 Gyr (Favata & Micela 2003). T Tauri stars are the most luminous stellar coronae observed, with X-ray luminosities of up to a few $10^{31} \text{ erg s}^{-1}$ while our Sun emits an average $\sim 10^{27} \text{ erg s}^{-1}$. The ROSAT all-sky survey was instrumental in showing that the number count of soft X-ray sources is dominated by stars at low galactic latitudes and that the vast majority of these stars are younger than about 1 Gyr (Guillout et al. 1996b). Compared to optical observations which require the measurement of relatively subtle age indicators such as photometric excess or lithium line equivalent width, soft X-ray surveys are thus an efficient and easy mean to map the spatial distribution of young stars up to relatively large distances. Some level of clustering and also large scale structures such as the Gould Belt are clearly visible in the X-ray sky (Guillout et al. 1998). Fundamental galactic parameters can be measured such as the increase of the scale height with age, presumably due to the diffusion of the galactic orbits by dynamical interactions with giant molecular cloud. The recent stellar formation rate can also be constrained from X-ray observations (Guillout et al. 1996a).

The best way to constrain these parameters is by generating X-ray population models and comparing their predictions with various observational results, such as $\log N(>S)$ - $\log S$ curves,

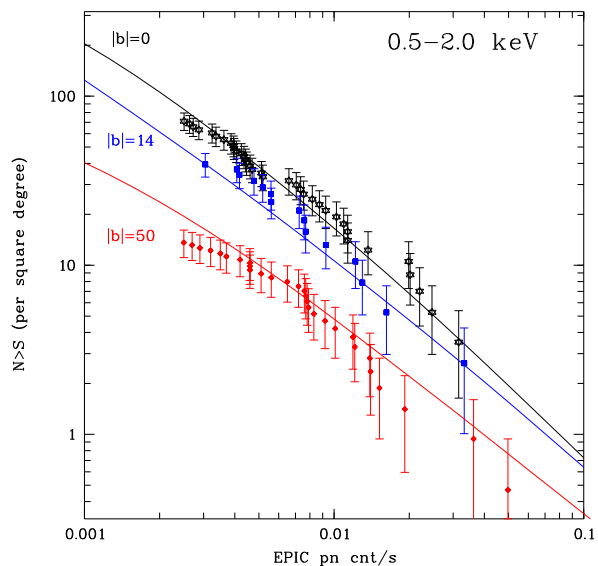


Fig. 8. The identified X-ray stellar $\log N(>S)$ - $\log S$ curves at low ($|b| = 0^\circ$: WR 110, Ridge 3 and GC2, black stars), mid ($|b| = 14^\circ$: GRB 001025 and Z And, blue squares) and high ($|b| = 50^\circ$: the AXIS sample, red lozenges) galactic latitudes. Thin lines represent the predictions of the stellar population models

but also distributions in magnitude, colours and distances. In the past, several X-ray models were designed (Rosner et al. 1981, Favata et al. 1992) which more or less all relied on the same ingredients, namely an underlying description of the stellar galactic population giving the distributions in position, distance, spectral type and age of the various stellar components (disc, thick disc, halo), age dependent X-ray luminosity functions, models for the interstellar absorption and instrumental response. In this work we will use an upgrade of the model developed by Guillout et al. (1996b) which was successfully applied to ROSAT data. A first adaptation of this model to XMM-Newton data has been presented in Guillout & Motch (2003). The underlying stellar distribution remains based on the Besançon model (Robin & Crézé 1986) and more precisely on its post-Hipparcos revision adjusted on optical and infrared (DENIS) counts (Robin et al. 2003). Changes in the temperatures of the thin thermal X-ray coronae with spectral types and age are now taken into account. The model also offers the possibility to handle more accurately the distribution of interstellar absorption in the line of sight. A detailed description of this model is presented in Guillout et al. (2006a, 2006b).

6.2. The stellar X-ray population

Fig. 8 shows the $\log N(>S)$ - $\log S$ curves derived from the optically identified X-ray stars, grouped in three bins of galactic latitude. The lower branch represents the contribution of the 33 stars with F_X (0.5-4.5 keV) brighter than $10^{-14} \text{ erg cm}^{-2} \text{ s}^{-1}$ identified in 17 of the deepest high galactic latitude AXIS fields (Barcons et al. 2002). The curve above is derived from all stel-

lar identifications in two mid-galactic latitude fields, namely GRB 001025 and Z And with a mean absolute galactic latitude of 14.2° . The upper curve is computed from the three $b \sim 0$ fields, WR 110, Ridge 3 and GC 2 with a mean absolute longitude of 10.6° . The density of identified stars sharply drops by a factor of ~ 2 by moving from $b = 0$ to 14° . Stellar population models show that the main effect is there, the change in latitude, the influence of moving away from the galactic center being much weaker (Guilout et al. 2006b). At the sensitivity limit of our survey, the density of identified active stars drops by a factor of ~ 5 between $b = 0^\circ$ and $b = 50^\circ$. This highlights the well known concentration of active coronae (mostly young stars at the flux sensitivity used in this survey) at low galactic latitudes. The thin lines in Fig. 8 represent the expected curves from the stellar population model. At low galactic latitude, we assume $l = 0^\circ$, $b = 0^\circ$, a best fit value of $A_V = 1.7$ mag/kpc (see below) and a limiting magnitude for optical identification of $R = 17$, slightly brighter than our expected optical limit. At mid-latitude we merge the models computed for the direction of each individual field assuming a cut in magnitude at $R=19$. For the high galactic sample we selected $b = 50^\circ$ and $l = 0^\circ$ a standard absorption and a limiting magnitude of $R=17$.

Both at low and high latitudes, the observed $\log N(>S)$ - $\log S$ curves match rather well those expected from X-ray count models provided the various biases, such as an enhanced absorption in the galactic plane and the limiting magnitude for optical identification are properly taken into account. Note that because of absorption prevailing at very low galactic latitudes, the actual number of stellar sources at $b \sim 0^\circ$ is likely underestimated (see below).

Figs 9 and 10 show the soft (0.5 - 2.0 keV; left panel) and hard (2.0-12 keV; right panel) bands $\log N(>S)$ - $\log S$ curves for the different fields analysed in this paper. In the soft band we assume energy to count factors (*ecf*) typical of active coronae at relatively low N_H . In the hard band, we use *ecf* suitable for absorbed AGN, apart for the $b \sim 0^\circ$ fields where we assume $N_H = 7.5 \cdot 10^{22} \text{cm}^{-2}$, typical of objects located in the region of the Galactic center.

Stars are mostly detected below 2 keV in agreement with their relatively soft mean temperature of 0.5 keV (Schmitt et al. 1990). The 0.5-2.0 keV curve for identified stars is the sum of the Z And and GRB 001025 fields (mean absolute galactic latitude of 14°) matches very well the model predicted curve taking into account the limiting magnitude of $R = 19$ for spectroscopic identification (see Tab. 7). This good agreement clearly indicates that we did not miss the identification of many stellar X-ray sources. At this latitude, stars account for less than 25% of the total number of sources above an X-ray flux of $5 \cdot 10^{-15} \text{erg cm}^{-2} \text{s}^{-1}$ (0.5 - 2 keV).

The field of PKS 0745 offset ($b = +3.3^\circ$) can be considered as an intermediate case since at the same flux limit of $5 \cdot 10^{-15} \text{erg cm}^{-2} \text{s}^{-1}$ the number of soft X-ray sources identified with stars represents about half of the total. Again, the model $\log N(>S)$ - $\log S$ curve, computed here assuming a limiting magnitude of $R = 21$ for spectroscopic identification, is roughly in agreement with the observed one. The statistical significance of the small excess of observed stars above $5 \cdot 10^{-15} \text{erg cm}^{-2} \text{s}^{-1}$ and of the deficit below this flux is not

very large. The origin of this possible discrepancy is unclear but could be due to the patchiness of the distribution of young stars in the line of sight.

Assuming a mean absorption of $A_V = 1$ mag/kpc provides a good fit to the total soft X-ray $\log N(>S)$ - $\log S$ curve in the field of GRO J1655-40. With a limiting magnitude of $R \sim 17$, slightly brighter than the one supposedly achieved, the difference between the identified $\log N(>S)$ - $\log S$ and total soft X-ray $\log N(>S)$ - $\log S$ curves can be easily accounted for. Because of the small number of sources and resulting low counting statistics, the absorption cannot be strongly constrained; however, a mean absorption above 2 mag/kpc is unlikely.

$\log N(>S)$ - $\log S$ curves for the very low latitude fields ($b \sim 0^\circ$) are shown in Fig. 10. In these directions, the soft X-ray source content is clearly dominated by the stellar component. Models with the standard absorption of $A_V = 0.7$ mag/kpc at $b = 0^\circ$ suitable for mid galactic longitudes, clearly overpredict the number of stars in these fields. In order to match the observed stellar $\log N(>S)$ - $\log S$ curve absorptions of $A_V = 1.2$ mag/kpc and $A_V = 2$ mag/kpc must be assumed in the WR110 + Ridge3 and GC2 fields respectively. Similar absorptions are seen towards low latitude objects such as open clusters and indeed rise towards the galactic center (Yoshi 2005). These absorptions are also consistent with those given by Arenou et al. (1992) for the solar environment. In general, our photometry is not accurate enough to trace the variation of absorption with distance by only using our sample of identified optical sources. We did not use the 3-D absorption model by Drimmel et al. (2003) because of its inaccuracy in the first kpc where most of identified coronal sources are located. Assuming these line of sight absorptions, the model $\log N(>S)$ - $\log S$ curve without cut in optical magnitude fits very well the curve obtained for the total sources. This good agreement shows that at very low galactic latitudes, the soft X-ray source content is completely dominated by the stellar component at the sensitivity of this survey. Interestingly, at a limiting magnitude of $R = 19$, we still miss 30% of the active coronae with a soft X-ray flux brighter than $5 \cdot 10^{-15} \text{erg cm}^{-2} \text{s}^{-1}$. A number of faint Me stars, but also of X-ray bright but absorbed active coronae of earlier spectral types fall below the magnitude limit. Our deep $H\alpha$ imaging indeed supports the idea that a large fraction of the error circles of unidentified soft sources with faint counterparts do contain $H\alpha$ emitting objects (Herent et al. 2003).

We show in Fig.11 the variation with galactic longitude of the density of soft sources in the low galactic latitude fields ($b < 4^\circ$). The point at $l = -50^\circ$ is derived from a specific X-ray survey extracted from the XMM-Newton archive (see Section 5 above and Fig. 15)). The low surface density at $l \sim 20^\circ$ reflects the clear deficit of soft sources in the G21.5-0.9 field compared to all other low latitude fields studied. It is likely that this particularly low density of soft sources is due to a pathological behaviour of the interstellar absorption in this direction. In particular, the nearby ($\sim 1.4^\circ$) field Ridge 3, absent from Fig. 11 because its shallowness does not reach $F_X = 4 \cdot 10^{-15} \text{erg cm}^{-2} \text{s}^{-1}$, does not show any significant deficit of soft sources compared to other low b fields. Finally, the surface density of hard X-ray sources in the field of G21.5-0.9 seems normal (see be-

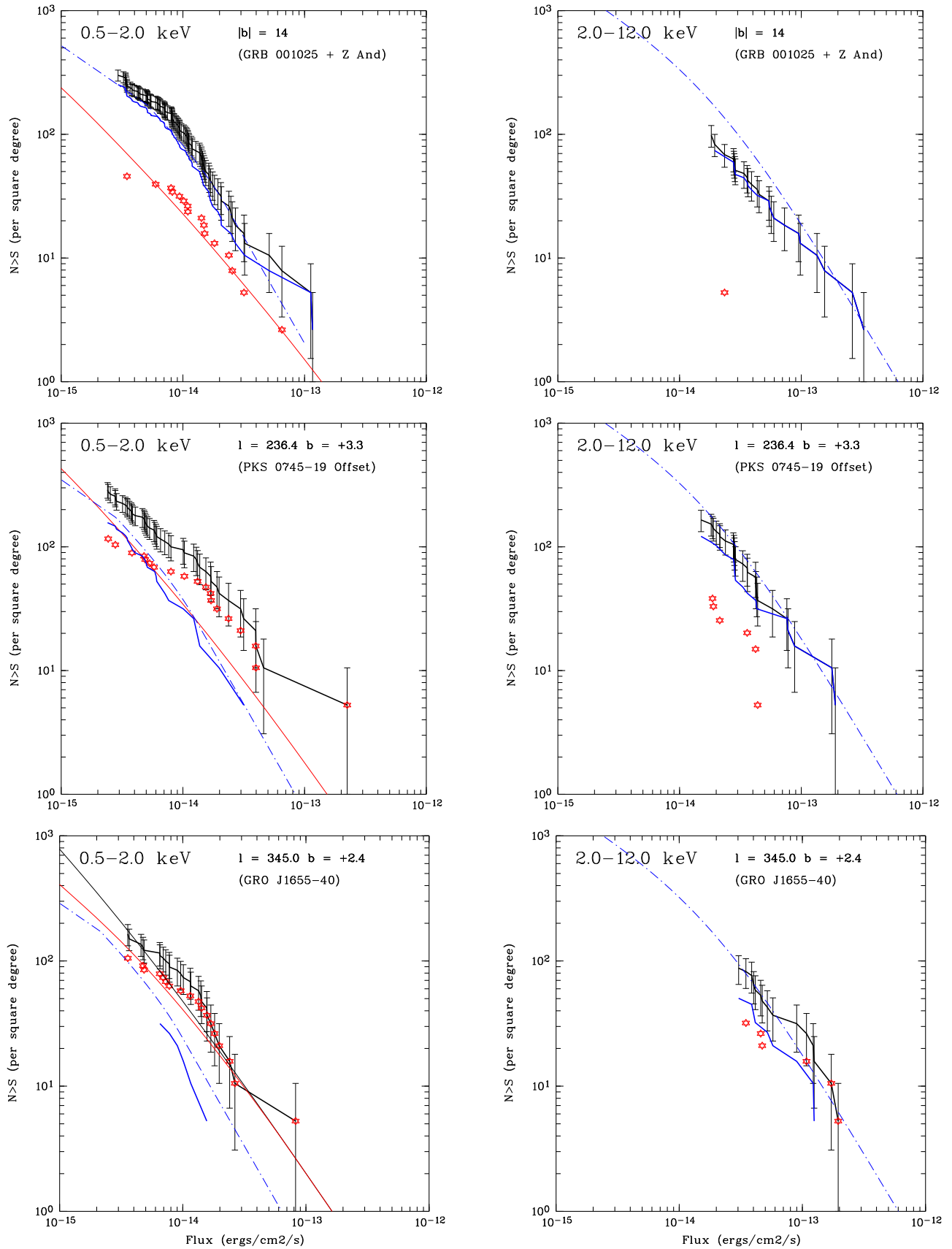


Fig. 9. Log $N(>S)$ -log S curves in the soft and hard bands for three directions surveyed in this work. Top panel, the combination of the Z And and GRB 001025 fields with a mean galactic latitude of 14° . Middle panel, the PKS 0745 offset field. Lower panel the field of GRO J1655-40. The black curves with error bars represent the total number of sources. Red stars show the log $N(>S)$ -log S curve for the identified active coronae. Thick blue lines display the sum of the identified extragalactic and unidentified sources. Thin black and red lines represent the model predicted curve for all active stars and for active stars brighter than the estimated limiting magnitude for optical identification. The dash dotted blue line show the expected extragalactic log $N(>S)$ -log S curve in the specified band and taking into account the total galactic absorption in the line of sight.

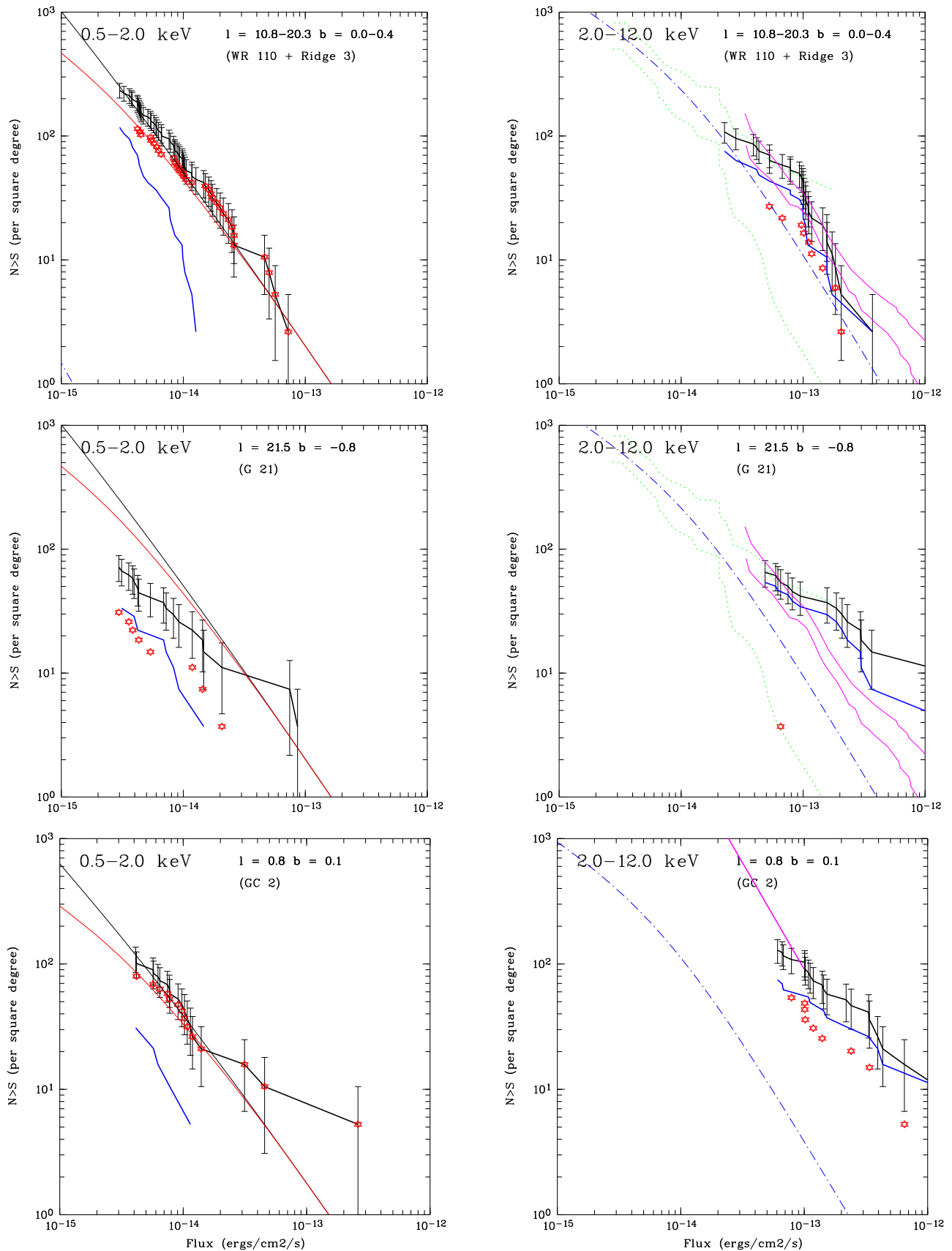


Fig. 10. Same as Fig. 9. Top panel, the sum of the WR 110 and Ridge 3 fields. Hard band, first two top panels; we plot as dotted green lines the Chandra $\log N(>S)$ - $\log S$ curve obtained by Ebisawa et al. (2001) from a deep Chandra pointing towards $l = 28.5^\circ$. The curve obtained by Hands et al. (2004) for XGPS data is drawn as thin purple lines in the first two top panels. Lower panel; the $\log N(>S)$ - $\log S$ curve derived by Munro et al. (2003) for the galactic center region shown as a thick purple line. Soft band, middle panel (G21.5-0.9 field); We show as comparison the best fit stellar population model $\log N(>S)$ - $\log S$ curves for the WR 110 + Ridge 3 fields to highlight the strong deficit of soft sources in this particular field. The density of hard sources is however normal. Stellar population models are shown here assuming an absorption of $A_V = 1.2$ mag/kpc (WR 110 + Ridge 3) and $A_V = 2$ mag/kpc (GC 2).

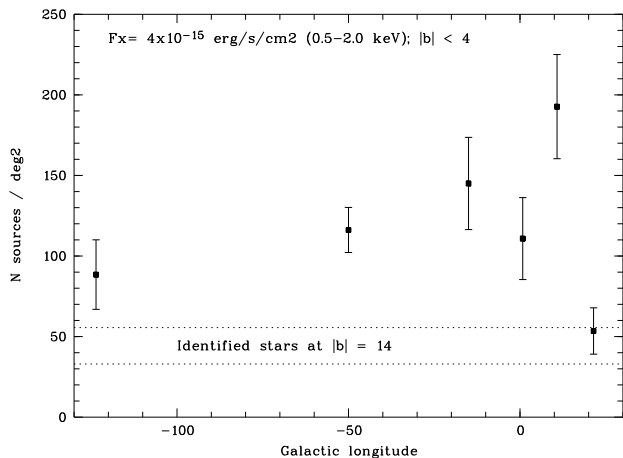


Fig. 11. Surface density of soft sources brighter than $4 \times 10^{-15} \text{ erg cm}^{-2} \text{ s}^{-1}$ in the soft band (mainly stellar coronae) as a function of galactic longitude for the low b fields ($|b| < 4^\circ$). The point at $l = -50^\circ$ is extracted from a specific group of XMM-Newton observations for which only statistical identification exists. The density of identified stars at higher galactic latitude ($|b| \sim 14^\circ$) is also shown for comparison.

low) giving further evidence for a local enhanced absorption. Interestingly, the standard stellar population model fails to fit the $\log N(>S)$ - $\log S$ curve even assuming very large absorption values of $A_V = 5 \text{ mag/kpc}$. A reasonably good fit can however be achieved assuming the presence of an absorbing wall with $A_V \sim 5$ located at $\sim 200 \text{ pc}$ (Guilout et al. 2006b). Such a distribution of the absorption on the line of sight in this direction is compatible with that derived from Neckel & Klare (1980) for that region.

Neglecting the G21.5-0.9 field, the average density of soft sources in the $|b| \leq 2.4^\circ$ fields does not vary much with longitude around a value of $136 \pm 8 \text{ deg}^{-2}$ at $F_X = 4 \times 10^{-15} \text{ erg cm}^{-2} \text{ s}^{-1}$ (0.5-2.0) keV. This mean density of soft sources, which is based on the predictions of the stellar model should be X-ray active stars in their vast majority, is about a factor 3 larger than the density of identified stars in the $|b| = 14^\circ$ average field (Z And + GRB 001025) and 1.5 times that of the PKS 0745 offset field at $b = 3.3^\circ$. Including the PKS 0745-019 offset region gives a weighted mean density of 120 deg^{-2} for $|b| \leq 3.3^\circ$.

We show in Fig. 12 the distribution in pn_HR2 of all sources and of the identified stellar sources having an error of less than 0.2 on the value of the hardness ratio. At very low galactic latitude, most soft sources are identified with stellar coronae. Based on the predictions of the stellar population model, we expect that the small fraction of unidentified soft sources is made of optically faint late type stars. Note that about 30% of the $|b| < 0.5^\circ$ sources have countrates which are too low in the 0.5-2.0 keV band ($0.7 \times 10^{-3} \text{ cts/s}$ on the average) to appear in this graph. The spread in pn_HR2 is rather large and probably due to significant interstellar absorption toward many active stars. This is consistent with the idea that we can detect and identify with relatively bright optical objects very young and X-ray luminous solar type stars up to rather large distances ($\geq 1 \text{ kpc}$). Both the enhanced interstellar absorption and the intrinsically

higher X-ray temperature of these young and very active coronae will contribute to harden the observed energy distribution. In comparison, the range of pn_HR2 values spanned by high galactic latitude active coronae appears narrower in agreement with their average older age and lower intrinsic coronal temperature and smaller interstellar absorption.

A number of stars are apparently detected above 2 keV, especially in the lowest galactic latitude regions. Although the latest version of the stellar population model applied here assumes a two temperature component thin thermal spectral model and takes into account its variation with spectral type and age, it is in all cases unable to predict the relatively large number of stars identified with sources detected above 2 keV (Guilout et al. 2006a). Part of the discrepancy could be due to the wrong association of a hard background source with an unrelated foreground optical object. Indeed, we expect that wrong stellar identifications will preferentially appear as hard sources. We believe, however, that the number of such stars is too high to be due to this effect only. It is more likely that we witness here the presence of a population which is not explicitly included in the stellar population model, such as that of old but active binaries (e.g. RS CVn stars). Finally, part of the effect could also be due to the scatter introduced by the statistical errors on photon counting in the hard bands which are not taken into account in the hardness ratio distribution predicted by the model, for instance.

6.3. The extragalactic component

The fraction of identified extragalactic X-ray sources dramatically varies with galactic latitude. The best identification rates are logically reached in the regions of highest latitudes observed with the most sensitive combination of instruments + telescope. In the low latitude fields, the total galactic absorption estimated from HI and infrared measurements reaches $N_H \sim 10^{23} \text{ cm}^{-2}$, equivalent to $A_V \sim 50$. Such a high interstellar absorption prevents the optical identification of any extragalactic source. The only low latitude extragalactic source is the cluster of galaxies found in the G21.5-0.9 field readily identified from its X-ray source extent and redshifted iron line. Another effect of the strong galactic absorption is the very significant X-ray spectral hardening of all background AGN which will mostly be detected above 2 to 4.5 keV. We thus expect that the dominating source population will strongly change with galactic latitude and energy band.

In the following we used for comparison the soft X-ray extragalactic $\log N(>S)$ - $\log S$ curve given by Hasinger et al. (1998) and at faint flux levels by Campana et al. (2001). In the hard band we assumed the $\log N(>S)$ - $\log S$ relation of Campana et al. (2001).

Fig. 9 shows that in the merged mid galactic latitude fields (GRB 001025 + ZAnd, $|b| = 14.2$, top panel), the identified extragalactic plus unidentified sources soft X-ray $\log N(>S)$ - $\log S$ curve matches remarkably well that expected for the extragalactic component taking into account the total galactic absorption in these directions. In the hard band, the expected extragalactic $\log N(>S)$ - $\log S$ curve lies slightly above the ob-

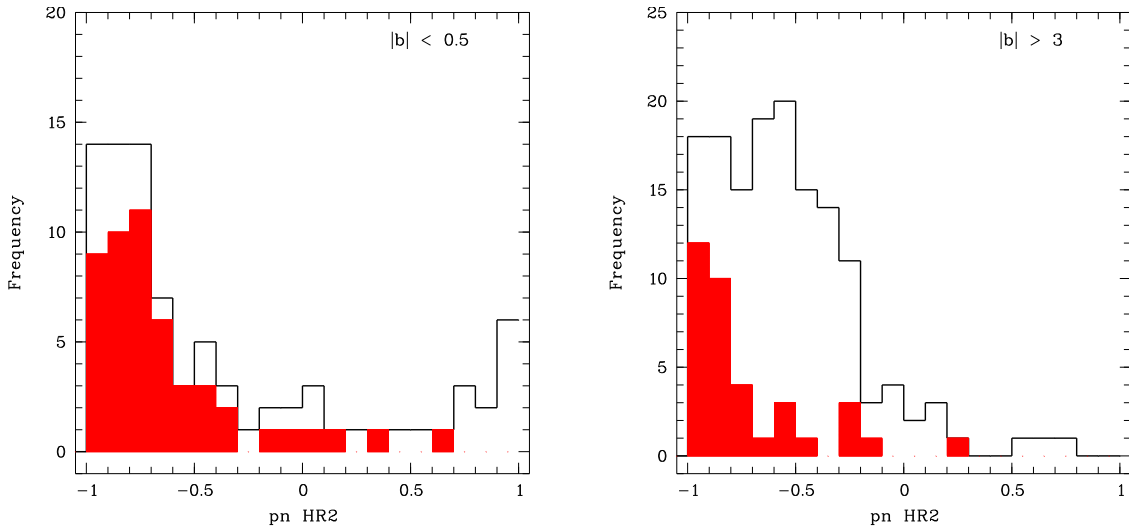


Fig. 12. Distribution in pn_HR2 of all sources (thick lines) and of the identified stars (filled histogram). Left panel: WR 110, Ridge 3 and GC2 low b fields; Right panel: PKS 0745 Offset, GRB 001025 and Z And high b fields. In all cases, only sources with $\text{err}(\text{pn_HR2}) < 0.2$ are considered.

served (mostly identified extragalactic + unidentified) curve. This discrepancy remains below the 2σ level down to $F_X = 5 \cdot 10^{-14} \text{erg cm}^{-2} \text{s}^{-1}$ and could be due in part to a problem in the correction of the sample effective area in this composite band and for these particular fields. At $|b| = 14.2$, the extragalactic component clearly dominates both the soft and hard X-ray source content, representing over 75% of the 0.5-2.0 keV sources above $5 \cdot 10^{-15} \text{erg cm}^{-2} \text{s}^{-1}$ and the totality of the 2.0-12.0 keV sample above $10^{-14} \text{erg cm}^{-2} \text{s}^{-1}$.

As mentioned in the previous section, the field of PKS 0745-19 offset at $b = 3.3^\circ$ and $l = 236.4^\circ$ (Fig. 9, mid panel) can be considered as an intermediate case. Again, the predicted soft extragalactic $\log N(>S)$ -log S curve fits that of the identified extragalactic + unidentified sample very well. In the hard X-rays, the total source sample can be accounted for by extragalactic sources only except for a few stars which have hard enough X-ray spectra show up above 2 keV. AGN represent about half of the soft sources detected in the 0.5-2.0 keV bands above $5 \cdot 10^{-15} \text{erg cm}^{-2} \text{s}^{-1}$.

The field of GRO J1655-40 ($b = 2.4^\circ$ and $l = 345^\circ$; Fig. 9, lower panel) is clearly dominated by the stellar component in the soft band. Still a large fraction of the unidentified soft sources should be background AGN. Our limiting R magnitude for spectroscopic identification (here $R = 19$) did not allow us to reach even the brightest AGN in this field of relatively high absorption ($N_H = 7.5 \cdot 10^{21} \text{cm}^{-2}$). In the hard 2.0-12.0 keV band, though, the situation does not differ from that seen in the previous fields since the extragalactic component can easily account for the vast majority of the sample.

At very low galactic latitude, galactic absorption efficiently shields the extragalactic background of sources at soft energies. Above 4.5 keV, the Galaxy becomes more or less transparent and AGN become detectable as strongly absorbed sources. In the 4.5-12 keV band for instance, the EPIC pn count rate of a typical AGN drops by only 23% when the line of sight absorption increases by 10^{23}cm^{-2} . Fig. 10 shows the $\log N(>S)$ -

log S curves in the very low galactic latitude fields (excluding the shallow field Ridge 4). The interstellar absorption is so high at these latitudes that all the AGN population is screened out in the soft energy range, the expected extragalactic soft $\log N(>S)$ -log S curve being orders of magnitude below that observed. The hard X-ray $\log N(>S)$ -log S curve lies significantly above that expected for the extragalactic component, the effect being marked mostly for the GC2 field, closest to the galactic center. In the WR 110 + Ridge 3 and G21.5-0.9 fields, the extragalactic background of sources contributes to $\sim 30\%$ of the total number of non-stellar sources brighter than $10^{-13} \text{erg cm}^{-2} \text{s}^{-1}$, while this fraction is less than 10% in the GC2 field.

6.4. A population of hard galactic X-ray sources

Our data strongly hint at the presence of a significant excess of hard sources above the expected extragalactic contributions at very low galactic latitude. This excess reveals the existence of a genuine population of galactic hard X-ray sources with relatively faint luminosities which in its large majority has escaped optical identification.

We list in Table 10 the surface density of hard galactic sources in two ways. First, attempting to remove the possible contribution of the tail of the X-ray active stars population with hard enough X-ray spectra to contribute above 2 keV, and second, a conservative estimate using the total density of hard sources. The true value may be in between the two estimates since a large fraction of the stellar identifications with hard sources is likely to be spurious. The expected extragalactic contributions are subtracted in all cases. We list these values for all fields optically searched in this project and for the additional fields used as comparisons. Whatever the measure adopted, there is a clear variation of the surface density of presumably galactic hard sources with galactic longitude. Fig. 13 highlights the rise of the density when approaching the cen-

ter of the Galaxy. The surface density of X-ray hard galactic sources seems to steadily rise from a very low value at $l = -50^\circ$ (see Fig. 15) to the peak value encountered close to the Galactic center crossing intermediate values at $l = 10^\circ$ - 20° . In the following we discuss separately the $l = 10^\circ$ - 20° and the $l \sim 0^\circ$ regions.

6.4.1. The $l = 10^\circ - 20^\circ$ region

An excess of hard X-ray sources of comparable amplitude has been reported by Hands et al. (2004) in the XGPS survey carried out at $l = 19^\circ$ - 22° and $b = \pm 0.6^\circ$. The XGPS consists of a group of relatively shallow dedicated pointings covering a total area of 3 deg² and comprising a total of ~ 400 sources. Note that two of the fields investigated in this paper, Ridge3 and Ridge4 are part of the XGPS. The XGPS $\log N(>S)$ - $\log S$ curve lies well above the expected absorbed extragalactic $\log N(>S)$ - $\log S$ curve and reveals a clear excess of hard galactic X-ray sources in the F_X range of $\sim (2 - 100) 10^{-14} \text{ erg cm}^{-2} \text{ s}^{-1}$ (2-10 keV).

We overplot in Fig. 10 the 2.0-10.0 keV XGPS $\log N(>S)$ - $\log S$ (scaled in the 2-12 keV band) on the merged WR 110 + Ridge 3 curve (mean galactic longitude of 15°) and on the G21.5-0.9 curve. The XGPS curve was corrected for the different intrinsic X-ray spectral shape used to convert count rates into fluxes. The agreement is excellent and confirms the existence of a modest but real population of hard X-ray galactic sources contributing above $\sim 5 10^{-14} \text{ erg cm}^{-2} \text{ s}^{-1}$ (2.0-12 keV) at $l \sim 20^\circ$. We also show for comparison on the same figure the $\log N(>S)$ - $\log S$ curve derived by Ebisawa et al. (2001) from a deep Chandra pointing towards $l = 28.45^\circ$. Chandra observations sample hard X-ray luminosities down to a few $10^{-15} \text{ erg cm}^{-2} \text{ s}^{-1}$, i.e., an order of magnitude below the sensitivity of XMM-Newton surveys. The surface density of the hard Chandra sources is only slightly higher than that measured in the high galactic latitude regions, indicating that the majority of the hard sources below $F_X \sim \text{a few } 10^{-14} \text{ erg cm}^{-2} \text{ s}^{-1}$ (2.0-12 keV) are background AGN.

As mentioned in the introduction, the XMM-Newton SSC has also carried out an identification campaign of X-ray bright sources among which are the 45 brightest XGPS sources in the broad (0.4-6 keV) band. Preliminary results of this study are presented in Motch (2005) and will be detailed in a forthcoming paper. In the F_X range between 10^{-12} and $10^{-13} \text{ erg cm}^{-2} \text{ s}^{-1}$ (2-10 keV), among 20 XGPS sources investigated, 8 have galactic counterparts (CVs, HMXRBs, very active stars, etc..) and 12 are possibly extragalactic with no optical identification brighter than $R \sim 23$. The figure of $\sim 40\%$ of galactic sources in this flux range is in good agreement with both the XGPS and SSC GPS $\log N(>S)$ - $\log S$ curves and confirms that in this range of X-ray flux, the galactic component of hard X-ray sources is probably dominated by accreting sources.

The expected number of CV in our survey is heavily dependent on the mean space density and on the shape of the X-ray luminosity function and to a lesser extent on the mean X-ray energy distribution considered. A local space density of $n \sim 3 \times 10^{-5} \text{ pc}^{-3}$ was derived from the analysis of the ROSAT Bright

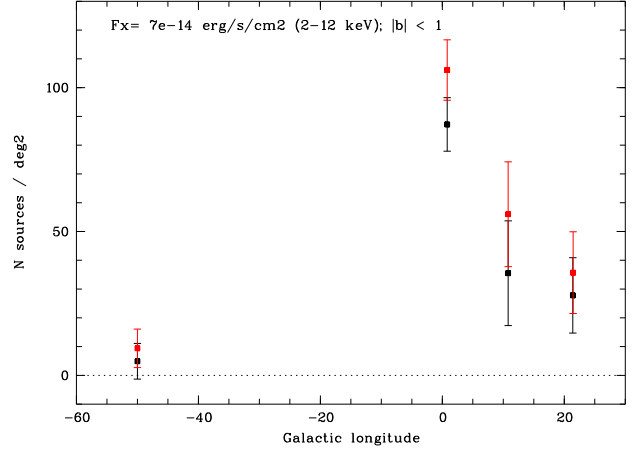


Fig. 13. Density of hard sources above the expected extragalactic contributions as a function of galactic longitude for the low b fields. Black: hard unidentified sources only; Red: all hard sources

Survey by Schwöpe et al. (2002) while Grindlay et al. (2005) argue in favor of a slightly lower value of $n \sim 1 \times 10^{-5} \text{ pc}^{-3}$. Watson (1999) has constructed $\log N(>S)$ - $\log S$ CV curves for various space densities and X-ray luminosity functions. In the $l = 10^\circ - 20^\circ$ regions, the density of unidentified sources is more compatible with $n = 1 \times 10^{-5} \text{ pc}^{-3}$ and $\langle L_X \rangle = 10^{31} \text{ erg s}^{-1}$ than with $n = 1 \times 10^{-6} \text{ pc}^{-3}$ and $\langle L_X \rangle = 10^{32} \text{ erg s}^{-1}$. The small size of any possible excess of hard sources in the fields at $l = -50^\circ$ apparent on Fig. 15 further favors a low spatial CV density. Averaging over the 9 fields studied optically, we would thus expect a total of ~ 15 CV brighter than $F_X = 10^{-13} \text{ erg cm}^{-2} \text{ s}^{-1}$ (2.0-12 keV). This number is obviously at variance with the one CV optically identified in the PKS 0745-19 offset field. However, the two XGPS CV found in the 10^{-12} and $10^{-13} \text{ erg cm}^{-2} \text{ s}^{-1}$ flux range have $R \sim 22$ and were optically identified using the ESO-VLT. It seems thus clear that the optical instrumentation used in the present survey, limited to $R \sim 21$, was not sensitive enough to identify the bulk of the cataclysmic variables.

6.4.2. The galactic center region

Several important structures populate the central $\pm 3^\circ$ of the Galaxy. The nuclear bulge (Mezger et al. 1996), not to be confused with the galactic bulge, is a flat disc-like structure of radius $\sim 230 \text{ pc}$, scale height $\sim 45 \text{ pc}$. It has a high density of stars and molecular gas and undergoes stellar formation. Its total mass is $\sim 1.4 10^9 M_\odot$ (Launhardt et al. 2002). In its center, lies the nuclear stellar cluster, a central concentration of stars with a R^{-2} distribution up to a radius of $\sim 30 \text{ pc}$. Several young massive clusters such as the Arches and the Quintuplet clusters are also found in the nuclear bulge.

The central region has been the target of all major X-ray telescopes such as, *Einstein*, GRANAT, ROSAT, BeppoSAX and ASCA. XMM-Newton and Chandra are now collecting deep observations of this area. Chandra has intensively observed the inner parts of the Galaxy. The first published survey is that of Wang et al. (2002) which covers about 0.8° in latitude,

Table 10. Density (in sources deg⁻²) of galactic hard (2-12 keV) sources at $F_X = 7 \cdot 10^{-14} \text{ erg cm}^{-2} \text{ s}^{-1}$

Field	l	$ b $	(Unidentified + EG) - EG	All - EG
PKS0745-19 off	-124.0	+3.3	-3.5 ± 12	-2.7 ± 12
GRB 001025 + Z And	173.5	+14.2	-12.8 ± 7.1	-12.8 ± 7.1
GRO J1655-40	-15.0	+2.4	-11.1 ± 10.0	4.7 ± 13.5
Gal.Plane	-50.0	0.2	4.9 ± 6.2	9.4 ± 6.7
GC 2	0.8	+0.1	55 ± 18.7	107.7 ± 25.7
GC 2+3+4+8	0.8	0.0	87.2 ± 9.3	106.1 ± 10.5
GC 10 + GRO J1744-28	0.0	0.3	37.2 ± 7.0	63.1 ± 8.6
WR 110	10.8	+0.4	35.5 ± 18.2	56 ± 18.2
G21.5-0.9	21.45	0.8	27.8 ± 13.1	35.7 ± 14.2

2° in longitude and is approximately centered on Sgr A*. About 800 new X-ray sources are detected in this area above a minimum flux of $\sim 10^{-14} \text{ erg cm}^{-2} \text{ s}^{-1}$ (2 - 8 keV) corresponding to a detection limit of $8 \times 10^{31} \text{ erg s}^{-1}$ at 8 kpc. The He-like Fe K α line mainly arises from the discrete sources. The number and the hard spectra of the discrete sources indicate the presence of numerous accreting white dwarfs, neutron stars or black holes in that region. Most of the X-ray flux is in the diffuse component which is apparently following known interstellar structures and may be related to regions of recent star formation.

Muno et al. (2003) have obtained a very long 590 ksec Chandra exposure centered on Sgr A*. The 17 by 17 arcminute ACIS-I field corresponds to a 40 pc \times 40 pc area at the distance of the galactic center and therefore essentially covers the nuclear stellar cluster. The survey completeness limit is $L_X \sim 10^{31} \text{ erg s}^{-1}$ at the distance of the galactic center. A total of 2357 sources were detected, mostly above 1.5 keV. Their radial distribution drops as θ^{-1} when moving away from Sgr A* and thus follows the infrared distribution of stars in the nuclear cluster. The density of faint hard sources is extremely high, being more than one order of magnitude above the expected extragalactic background of sources. Their X-ray spectra are very hard with power law photon index below 1.0 and exhibit strong lines from low ionization, He-like and H-like iron. Some of these sources display variability on day or month time scales (Muno et al. 2004). Both spectral and timing properties are compatible with magnetically accreting white dwarfs and wind accreting neutron stars. On the other hand, soft sources are uniformly distributed on the sky as expected from a local stellar population.

It is clear from Fig. 10 and Table 10 that the excess of hard sources above the extragalactic background in the GC2 field ($l = 0.8^\circ$), is much higher than in the $l = 10^\circ - 20^\circ$ region. The series of 'GC' fields allows us to study the spatial distribution of the hard sources in the central regions and check whether the excess of hard sources we see in GC 2 is also present in nearby fields. Fig. 14 (top panel) displays the log N(>S)-log S curves derived from XMM-Newton fields GC2, GC3, GC4 and G8 which have a mean absolute longitude of 0.8° and are centered at exactly $b = 0^\circ$. The excess of hard galactic X-ray sources seen in the GC2 field is also clearly present in the adjacent $b = 0^\circ$ areas, larger than found for the XGPS at $l = 20.5^\circ$ but below the extreme densities encountered in the nuclear central cluster (Muno et al. 2003; see Fig. 14). At a 2-12 keV flux of $\sim 7 \cdot 10^{-14} \text{ erg cm}^{-2} \text{ s}^{-1}$, corresponding to $L_X \sim 5 \cdot 10^{32} \text{ erg s}^{-1}$ at

8 kpc, the source density at $|l| \sim 0.8^\circ$ is $\sim 110 \text{ deg}^{-2}$, i.e., about 2 times that observed in the XGPS or in the G21.5-0.9 fields at $l = 20^\circ$. The galactic over extragalactic hard sources contrast is highest for the GC 2+3+4+8 fields, with an estimated extragalactic contribution amounting to only $\sim 10\%$ of the total of hard sources. The density of unidentified hard galactic sources (see Tab. 10) is 3 times larger at $|l| = 0.8^\circ$ than at $l = 21.5^\circ$. We do not see, however, any evidence of variation of the source density with longitude within the GC2, GC3, GC4 and GC 8 pointings.

In comparison, the density of soft, likely stellar and therefore relatively local sources ($d < 2 \text{ kpc}$), is again consistent with the expectations of the stellar population models if one assumes a mean absorption of $A_V = 2 \text{ mag/kpc}$, slightly higher than that needed for the $l = 10^\circ - 20^\circ$ regions, but identical to that used in the GC 2 field alone. Although the total absorption in the GC2 field is slightly lower than towards Sgr A*, it is still very high ($3.4 - 7.5 \cdot 10^{23} \text{ cm}^{-2}$) and severely hampers optical identifications. The optical wavelength and the medium size (4-m) of the telescope used for this project did not allow us to identify any of the hard sources while the majority of the soft sources were positively identified with F-K + Me stars. Although we do not have optical spectroscopic identifications at the telescope, the hardness ratio distribution of the sources having a likely USNO-A2.0 match in the "GC series" fields (see Fig. 7) points toward similar conclusions. This picture is consistent with the idea that all sources detected in this direction at $F_X(0.5 - 2.0 \text{ keV}) \geq 5 \cdot 10^{-15} \text{ erg cm}^{-2} \text{ s}^{-1}$ are nearby active coronae.

Fig. 14 (lower panel) also shows the log N(>S)-log S curve derived from the two XMM-Newton pointings north and south of Sgr A*, GRO J1744 and GC10, which have a mean galactic latitude of $|b| = 0.33^\circ$ (corresponding to 46 pc at 8 kpc). At $|b| = 0.33^\circ$, the density of unidentified hard galactic sources is about half of that at $|b| = 0.0$ for $F_X = 7 \cdot 10^{-14} \text{ erg cm}^{-2} \text{ s}^{-1}$ (see Table 10). On the other hand, the density of soft sources remains almost unchanged, as expected from the small change in galactic latitude. The best fit stellar population model assumes $A_V = 1.5 \text{ mag/kpc}$, a somewhat lower absorption than toward the $b = 0.0^\circ$ direction. If confirmed, for instance by a detailed analysis of the Wang et al. (2002) Chandra survey, this steep density drop with galactic latitude may indicate that the majority of the hard sources has an origin in the nuclear bulge which has a scale height of $\sim 45 \text{ pc}$.

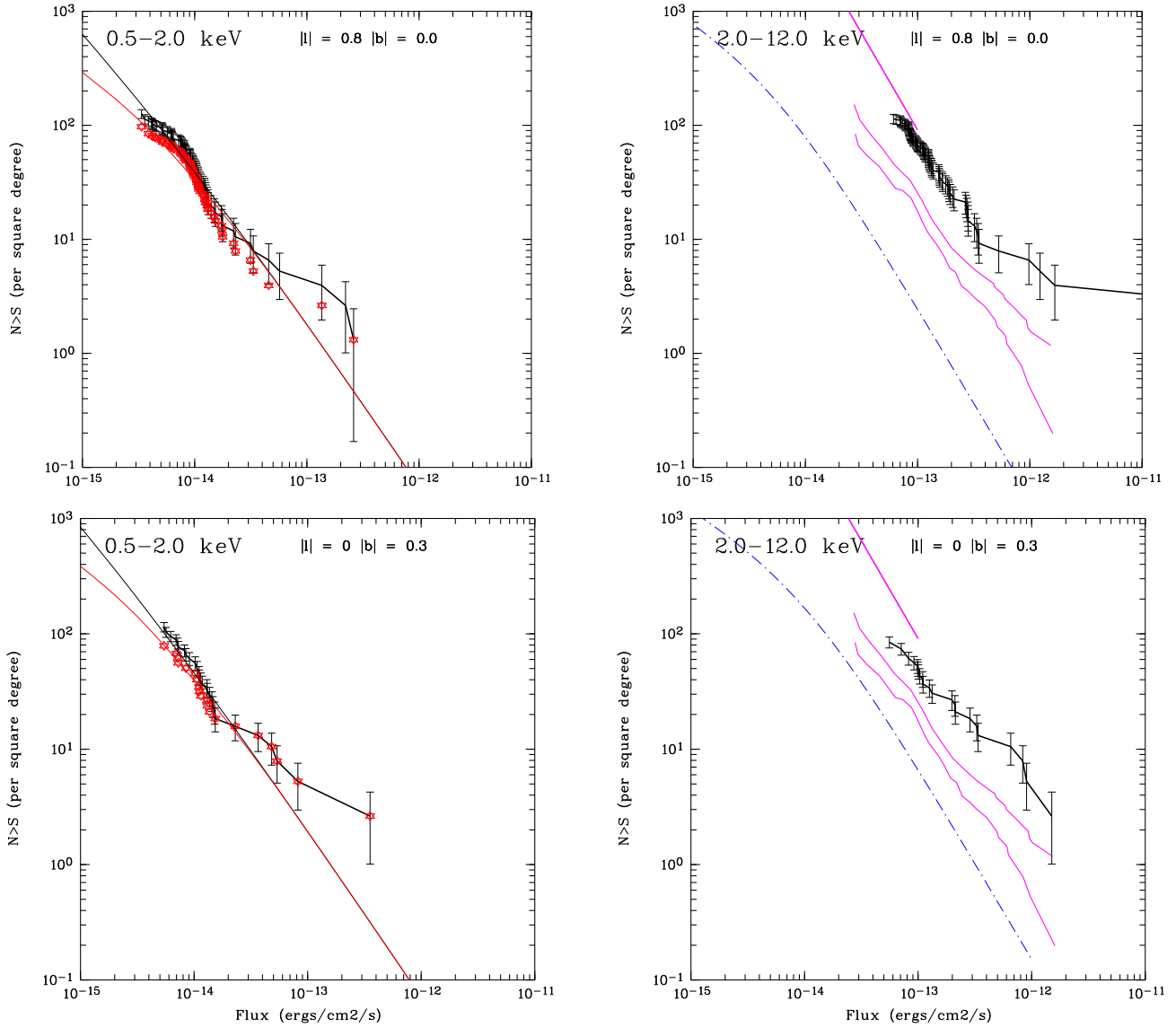


Fig. 14. Log $N(>S)$ -log S curves in the hard and soft bands for a group of low galactic latitude regions located close to the Galactic Center. Red star symbols show the statistically identified stellar contribution. In the soft bands the thin black line represents the best total stellar model assuming $A_V = 2.0$ mag/kpc for the $b = 0.0^\circ$ direction and $A_V = 1.5$ mag/kpc for the $|b| = 0.3^\circ$ region. In both cases, the red line shows the corresponding models assuming a limiting magnitude of $R \sim 17$. In the hard bands, the expected extragalactic log $N(>S)$ -log S curve appears as a dash-dotted line. The thick purple line shows the curve obtained by Munro et al. (2003) for a small area around the Galactic Center and the thin line, densities observed in the XGPS by Hands et al. (2004).

The nature of the hard X-ray sources detected in the nuclear bulge and in the central nuclear cluster remains elusive. The high interstellar absorption and source crowding make infrared identification difficult, even in the small Chandra error circles. Most of the sources are faint in X-rays and do not allow detailed X-ray spectroscopy or light curve analysis. Munro et al. (2004) have however found intra-day or inter-month variability, which together with their spectral properties point at a population of magnetically accreting white dwarfs or wind accreting neutron stars. Deep infrared imaging shows that massive X-ray binaries are unlikely to account for the majority of the sources in the nuclear cluster (Laycock et al. 2005). Bandyopadhyay

et al. (2005) find K band counterparts for $\sim 75\%$ of a sample of sources in the nuclear bulge region surveyed by Wang et al. (2002) ($F_X \geq 4 \cdot 10^{-14}$ erg $\text{cm}^{-2} \text{s}^{-1}$) suggesting a population of highly reddened stars.

7. Conclusions

We present first results from an ongoing observational project aimed at the identification of serendipitous XMM-Newton sources in the galactic plane. Optical identifications are carried out using ESO, Canary Islands, CFHT and OHP telescopes and involve deep wide field multi colour imaging and follow up spectroscopy of optical candidates. The galactic landscape

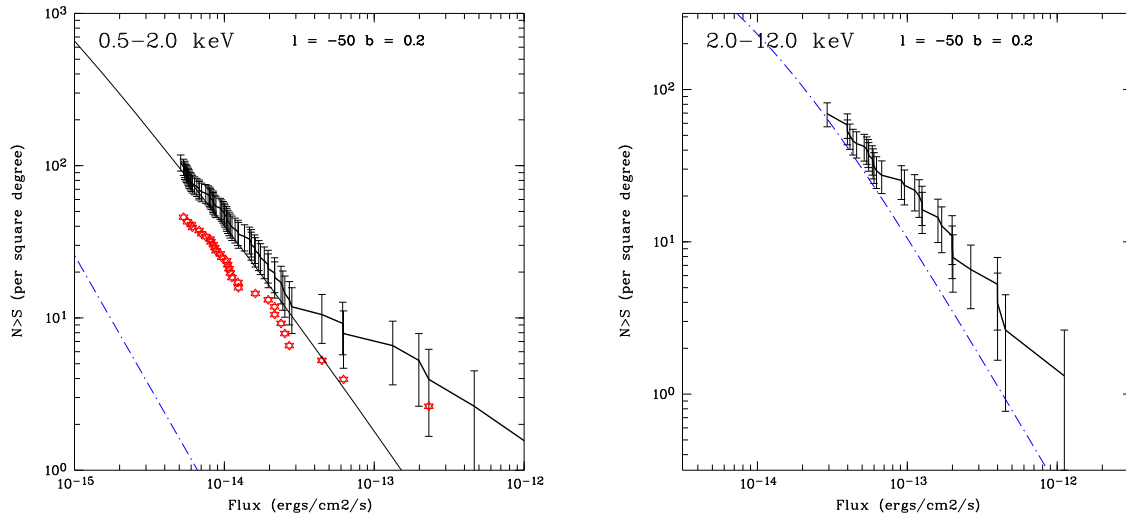


Fig. 15. Log $N(>S)$ -log S curves in the hard and soft bands for low galactic latitude regions located at $l \sim -50^\circ$. Red star symbols show the statistically identified stellar contribution and blue dash-dotted lines the expected extragalactic contribution. In the soft bands the thin black line represents the best total stellar model assuming $A_V = 1.5$ mag/kpc.

unveiled by XMM-Newton differs significantly from that delivered by ROSAT. First, the good sensitivity of the EPIC camera of XMM-Newton above 2 keV permits the discovery of all the faint and hard sources which were not accessible to ROSAT. Among these faint flux hard sources we expect to find the low X-ray luminosity accreting binaries such as cataclysmic variables, X-ray transients in the low state and possibly other species of yet to be discovered low mass transfer rate stages predicted by the evolutionary theories of bright low and high-mass X-ray binaries. Second, the large soft X-ray collecting effective area allows us to probe the population of soft galactic sources up to distances of about 3 times larger than that possible with ROSAT, thus offering a view on the spatial distribution of the young stellar population to distances as large as ~ 1 kpc.

Our optical identification program is limited by the optical wavelength used which does not allow us to observe X-ray source counterparts shrouded in the deep layers of galactic absorption. Another limitation arises from the 4-m class telescope used which limit optical spectroscopy to $R \sim 21$. The result of our observational effort reflects these limitations. We identify most soft X-ray sources with active stars. The fraction of positively identified extragalactic sources increases with increasing galactic latitude. Most hard X-ray sources remain unidentified. Among the optically identified hard sources are a CV and a group of Be stars with properties very similar to those of the so far unique star γ -Cas. We argue that these Be stars could harbour an accreting white dwarf, as predicted by evolutionary models. Alternatively, as proposed for γ -Cas, the hard X-ray emission could be due to magnetic interaction of the star with the circumstellar disc.

The surface density of active coronae drops sensitively with increasing galactic latitude, but does not vary much with longitude. Log $N(>S)$ -log S curves are generally in good agreement with the predictions of the X-ray stellar population model, thus indicating that its main ingredients, in particular, the scale

heights used for the various stellar ages are likely to be close to their actual values. However, patchiness of the interstellar medium makes detailed comparison somewhat difficult at low latitudes. In the field of G21.5-0.9, for instance, we observe a number of soft sources significantly lower than in other nearby fields while the density of hard sources remains similar to that seen at comparable longitudes and latitudes. We interpret this as the signature of a strong local absorption in this particular direction.

At a 2-12 keV flux of 7×10^{-14} erg cm $^{-2}$ s $^{-1}$, and $|l| \leq 20^\circ$, the surface density of hard sources of non coronal nature exceeds that of the extragalactic background by a significant amount. This excess is the signature of the presence of a genuine population of low luminosity ($L_X \sim 10^{33}$ erg s $^{-1}$) galactic sources. Interestingly, the hard source density steadily increases toward the galactic center ($|l| \sim 0.8^\circ$ $b = 0.0^\circ$) where it can amount to up to ten times the background of AGN. At this position the density of hard unidentified sources reaches ~ 90 sources deg $^{-2}$ at $F_X = 7 \times 10^{-14}$ erg cm $^{-2}$ s $^{-1}$. Close to the galactic center, the hard source density seems to show a strong dependency on latitude since it decreases by a factor of ~ 2 at $|b| = 0.3^\circ$. If confirmed by other observations, this latitude dependency could constitute strong evidence for an origin in the nuclear bulge.

We are pursuing our optical identification campaign in several other fields with the aim to better sample the range of galactic latitude and longitudes. These new X-ray and optical data will provide us with a more accurate view on the various populations of low luminosity X-ray sources unveiled by XMM-Newton.

Acknowledgements. We thank R. Lopes de Oliveira and I. Negueruela for help in analysing optical and X-ray data of the Be/X-ray candidates. We acknowledge support by the Deutsches Zentrum für Luft- und Raumfahrt (DLR) under contract FKZ 50 OX 0201. This research

has made use of the SIMBAD database and of the VizieR catalogue access tool operated at CDS, Strasbourg, France.

References

- Arenou, F., Grenon, M., Gomez, A. 1992, *A&A*, 258, 104
- Bandyopadhyay, R.M., Miller-Jones, J.C.A., Blundell, K.M., et al. 2005, *MNRAS*, in press, astro-ph/0509346
- Barcons, X., Carrera, F.J., Watson, M.G., et al., 2002, *A&A*, 382, 522
- Berghöfer, T.W., Schmitt, J.H.M.M., Danner, R., & Cassinelli, J.P. 1997, *A&A*, 322, 167
- Campana, S., Moretti, A., Lazzati, D., & Tagliaferri, G. 2001, *ApJ*, 560, L19
- Cassinelli, J.P., Cohen, D.H., MacFarlane, J.J., Sanders, W.T., Welsh, Y. 1994, *ApJ*, 421, 705
- Dame, T.M., Hartmann, D., Thaddeus, P. 2001, *ApJ*, 547, 792
- Dickey, J. M., Lockman, F. J. 1990, *Ann. Rev. Astron. Astrophys.*, 28, 215
- Drimmel, R., Cabrera-Lavers, A., López-Corredoira, M. 2003, *A&A*, 409, 205
- Ebisawa, K., Maeda, Y., Kaneda, H., & Yamauchi, S. 2001, *Science*, 293, 1633
- Ebisawa, K., Tsujimoto, M., Paizis, A., et al. 2005, *ApJ*, 635, 214
- Favata, F., Micela, G., Sciortino, S., Vaiana, G. S. 1992, *A&A*, 256, 86
- Favata, F., Micela, G. 2003, *SSRv*, 108, 577
- Guillout, P. 1996a, PhD, Observatoire Astronomique de Strasbourg, Universit Louis Pasteur, France
- Guillout, P., Haywood, M., Motch, C., & Robin, A. C. 1996b, *A&A*, 316, 89
- Guillout, P., Sterzik, M. F., Schmitt, J. H. M. M., Motch, C., Neuhaeuser, R. 1998, *A&A*, 337, 113G
- Guillout, P., Schmitt, J. H. M. M., Egret, D., et al. 1999, *A&A*, 351, 1003
- Guillout, P., & Motch, C. 2003, *Astronomische Nachrichten*, 324, 81
- Guillout, P., Herent, O., Motch, C. 2006a, in proceedings of the "X-ray Universe 2005" El Escorial, Madrid, Spain, 26-30 September 2005, ESA SP-604, p89
- Guillout et al. 2006b, in preparation
- Grindlay, J.E., Hong, J., Zhao, P., et al. 2005, *ApJ*, 635, 920
- Hands, A.D.P., Warwick, R.S., Watson, M.G., Helfand, D.J. 2004, *MNRAS*, 351, 31
- Hasinger, G., Burg, R., Giacconi, et al. 1998, *A&A*, 329, 482
- Herent, O., Motch, C., Warwick, R., Wheatley, P., Guillout, P. 2003, *AN*, 342, 142
- Herent, O., Motch, C., Guillout, P. 2005, in proceedings of the "X-ray Universe 2005" El Escorial, Madrid, Spain, 26-30 September 2005, ESA SP-604, p91
- Jacoby, G., Hunter, D., Christian, C. 1984, *ApJSS*, 56, 257
- Jascheck, C. & Jascheck, M. 1987, "The Classification of Stars", Cambridge University Press
- Kubo, S., Murakami, T., Ishida, M., Corbet, R.H.D. 1998, *PASJ*, 50, 417
- Launhardt, R., Zylka, R., Mezger, P. G. 2002, *A&A*, 384, 112
- Laycock, S., Grindlay, J., van den Berg, M., et al. 2005, *ApJ*, in press
- Lopes de Oliveira, R., Motch, C., Haberl, F., Negueruela, I., Janot-Pacheco, E. 2006, *A&A*, in press.
- Marco, A., Negueruela, I., & Motch, C. 2006, in Moffat, A.F.J., & St.-Louis, N. (eds.), Proceedings of Massive Stars in Interacting Binaries, Hotel Sacacomie, Montreal, Quebec, Canada, August 2004, ASP Conference Series, in press
- Michel, L., Herent, O., Motch, C., Pye, J., Watson, M. G. 2004, (ADASS) XIII, Proceedings of the conference held 12-15 October, 2003 in Strasbourg, France. Edited by Francois Ochsenbein, Mark G. Allen and Daniel Egret. ASP Conference Proceedings, Vol. 314, p.570
- Morley, J. E., Briggs, K. R., Pye, et al. 2001, *MNRAS*, 326, 1161
- Motch, C., Guillout, P., Haberl, F., et al. 1997a, *A&A*, 312, 111
- Motch, C., Haberl, F., Dennerl, K., Pakull, M., & Janot-Pacheco, E. 1997b, *A&A*, 323, 853
- Motch, C. 2000, ASP Conf Series 232, p16
- Motch, C., Barcons, X., Carrera, F., et al., 2002, (astro-ph/0203025), in Proceedings of the Symposium on 'New Visions of the X-ray Universe in the XMM-Newton and Chandra Era', 26-30 November 2001, ESTEC, The Netherlands
- Motch C. et al. 2003, *AN*, 324, 51
- Motch, C. 2005 in proceedings of the "X-ray Universe 2005" El Escorial, Madrid, Spain, 26-30 September 2005, ESA SP-604, p383
- Motch, C., Lopes de Oliveira, R., Negueruela, I., Haberl, F., Janot-Pacheco, E. 2006, in proceedings of the conference on Active O-B stars, Sapporo, Sept 2005, ASP Conference Series, Eds S. Stefl, S. Owocki and A. Okazaki.
- Muno, M.P., Baganoff, F.K., Bautz, et al. 2003, *ApJ*, 589, 225
- Muno, M.P., Arabadjis, J.S., Baganoff, F.K., et al. 2004, *ApJ*, 613, 1179
- Neckel, T., Klare, G., & Sarcander, M. 1980, *A&AS*, 42, 251
- Negueruela, I. 1998, *A&A*, 338, 505
- Nevailanen, J., Lumb, D., dos Santos, S. et al. 2001, *A&A* 374, 66
- Ochsenbein F., Bauer P., Marcout J. 2000, *A&AS* 143, 221
- Pfahl, E., Rappaport, S., Podsiadlowski, P. 2002, *ApJ*, 571, L37
- Raguzova, N., 2001 *A&A*, 367, 848
- Robin, A., Crézé, M. 1986, *A&A*, 157, 71
- Robin, A. C., Reyl, C., Derrire, S., Picaud, S. 2003, *A&A*, 409, 523
- Robinson, R.D., Smith, M.A., Henry, G.W. 2002, *ApJ*, 575, 435
- Rosner, R., Avni, Y., Bookbinder, et al. 1981, *ApJ*, 249, L5
- de Ruiter, H. R., Arp, H. C., & Willis, A. G. 1977, *A&AS*, 28, 211
- Schlegel, D. J., Finkbeiner, D. P., Davis, M. 1998, *ApJ*, 500, 525
- Schwöpe, A. D., Brunner, H., Buckley, D., et al.. 2002, *A&A*, 396, 895
- Schmitt, J. H. M. M., Collura, A., Sciortino, S., et al. 1990, *ApJ*, 365, 704
- Stelzer, B., Huélamo, N., Hubrig, S., Zinnecker, H., & Micela, G. 2003, *A&A*, 407, 1067
- Sugizaki, M., Mitsuda, K., Kaneda, H., et al. 2001, *ApJS* 134, 77
- Torrejon, J.M., & Orr, A. 2001, *A&A*, 377, 148
- Turner, D.G. 1981, *AJ*, 86, 231
- Turnshek, D.E., Turnshek, D.A., Craine, R.E., Boeshaar, P.C. 1985 "An Atlas of Digital Spectra of Cool Stars", Western Research Company
- Vaiana, G. S., Cassinelli, J. P.; Fabbiano, G., et al. 1981, *ApJ*, 245, 163
- Walker, A.R., Laney, C.D. 1987, *MNRAS*, 224, 61
- Wang, Q.D., Gotthelf, E.V., Lang, C.C. 2002, *Nature*, 415, 148
- Watson, M.G. 1999, ASP Conference Series, Volume 157, edited by Coel Hellier and Koji Mukai, p. 291
- Watson, M. G, Augures, J.-L., Ballet, J. et al., 2001, *A&A* 365, L51
- Watson, M. G, Pye, J.P., Denby, et al. 2003, *AN*, 342, 89
- Wheatley, P. J. 1998, *MNRAS*, 297, 1145
- Wijnands, R., in't Zand, J.J.M., Rupen, et al. 2005, *A&A*, in press.
- Willems, B., Kolb, U. 2003, *MNRAS*, 343, 949
- Yoshi, Y.C. 2005 *MNRAS*, 362, 1259
- Yuan, W., McMahon, R.G., Watson, M., et al. 2003, *AN*, 324, 178

Table 11. PKS 0745-19 offset

Src Num	Source Name	RA (J2000)	DEC (J2000)	r90 arcsec	pn countrate cts/s	error cts/s	pn HR2	pn HR2 error	Class	R	Type	Optical Id
1	1XMM J074857.5-190632	07 48 57.46	-19 06 32.5	1.1	.158	.003	-0.92	0.01	AC	13.99	M4Ve	S102202212853 GSC2
7	1XMM J074734.5-185656	07 47 34.55	-18 56 56.0	1.5	.032	.002	-0.32	0.07	EG	20.00	AGN	
4	1XMM J074743.5-185654	07 47 43.55	-18 56 53.5	1.2	.030	.002	-0.73	0.05	XRB	20.78	CV	
6	1XMM J074832.1-185427	07 48 32.07	-18 54 27.2	1.2	.026	.002	-0.89	0.05	AC	13.43	G2V	S102202218280 GSC2
2	1XMM J074818.7-191732	07 48 18.72	-19 17 31.7	1.2	.026	.002	-0.80	0.04	AC	14.23	G9Ve	S102202320236 GSC2
15	1XMM J074722.6-190700	07 47 22.64	-19 07 00.3	2.0	.019	.002	-0.68	0.08	AC	14.88	G9Ve	S102202329046 GSC2
3	1XMM J074847.1-190410	07 48 47.12	-19 04 10.4	1.3	.016	.001	0.66	0.14	EG	18.98	AGN	
5	1XMM J074823.2-190937	07 48 23.16	-19 09 37.4	1.1	.016	.001	-0.93	0.03	AC	13.95	G9Ve	S102202327003 GSC2
74	1XMM J074824.7-190734	07 48 24.66	-19 07 34.2	1.5	.014	.002	-0.73	0.12	AC	14.34	G3V	S102202328656 GSC2
28	1XMM J074718.3-190524	07 47 18.26	-19 05 24.2	3.1	.014	.002	-0.85	0.12	*	*	*	
11	1XMM J074902.5-191253	07 49 02.48	-19 12 52.7	1.4	.014	.001	-0.32	0.10	*	*	*	
19	1XMM J074849.7-191705	07 48 49.67	-19 17 04.6	1.5	.013	.001	-0.24	0.11	EG	20.22	AGN	
8	1XMM J074829.1-191641	07 48 29.07	-19 16 41.4	1.5	.012	.001	-0.96	0.05	AC	*	F4V	TYC 5989-861-1
10	1XMM J074806.1-190857	07 48 06.10	-19 08 56.7	1.3	.010	.001	-0.42	0.08	EG	21.18	AGN	
18	1XMM J074855.2-185824	07 48 55.23	-18 58 23.9	1.5	.010	.001	-0.90	0.08	AC	15.97	K4Ve	S102202216278 GSC2
17	1XMM J074901.2-185826	07 49 01.18	-18 58 26.2	1.7	.010	.001	-1.00	0.06	AC	13.43	G9Ve	S102202216266 GSC2
21	1XMM J074739.6-190734	07 47 39.64	-19 07 34.4	1.8	.009	.001	-0.91	0.05	AC	13.96	G3V	S102202328660 GSC2
22	1XMM J074825.1-185550	07 48 25.05	-18 55 50.1	1.5	.009	.001	0.18	0.15	EG	19.99	AGN	
20	1XMM J074852.5-185857	07 48 52.54	-18 58 56.9	1.5	.008	.001	-0.55	0.10	EG	22.57	AGN	
26	1XMM J074826.0-191732	07 48 25.98	-19 17 32.1	2.3	.007	.001	-0.91	0.10	AC	*	A4III	HD 63482
12	1XMM J074805.6-190506	07 48 05.61	-19 05 05.8	1.3	.007	.001	-0.30	0.10	EG	21.65	AGN	
53	1XMM J074906.7-185815	07 49 06.67	-18 58 14.7	1.7	.006	.001	-0.29	0.25	*	*	*	
33	1XMM J074737.5-185944	07 47 37.55	-18 59 43.7	1.7	.006	.001	-0.34	0.14	*	*	*	
24	1XMM J074830.3-191348	07 48 30.31	-19 13 48.4	1.7	.006	.001	-0.21	0.14	*	*	*	
62	1XMM J074732.1-190209	07 47 32.11	-19 02 08.8	7.9	.006	.001	1.00	2.12	*	*	*	
47	1XMM J074815.4-191417	07 48 15.43	-19 14 17.0	1.7	.006	.001	-0.11	0.17	AC	17.87	K1V	S102202322991 GSC2
29	1XMM J074905.1-190036	07 49 05.06	-19 00 35.8	2.0	.005	.001	-0.88	0.08	AC	17.19	M5Ve	
48	1XMM J074737.0-190247	07 47 36.96	-19 02 47.3	4.4	.005	.001	-0.26	0.21	*	*	*	
30	1XMM J074828.9-191512	07 48 28.95	-19 15 12.1	1.8	.005	.001	-0.43	0.14	*	*	*	
56	1XMM J074804.4-185623	07 48 04.37	-18 56 23.4	1.9	.005	.001	-0.21	0.19	*	*	*	
23	1XMM J074842.9-190342	07 48 42.93	-19 03 42.0	1.9	.005	.001	-0.11	0.14	*	*	*	
54	1XMM J074742.1-190743	07 47 42.06	-19 07 42.6	4.1	.004	.001	-0.67	0.15	*	*	*	
65	1XMM J074814.3-191751	07 48 14.32	-19 17 51.1	2.1	.004	.001	-0.29	0.23	*	*	*	
46	1XMM J074740.2-190104	07 47 40.23	-19 01 04.3	2.1	.004	.001	-0.49	0.16	*	*	*	
36	1XMM J074747.9-190315	07 47 47.86	-19 03 15.1	2.7	.004	.001	-0.33	0.19	*	*	*	
25	1XMM J074819.9-190149	07 48 19.87	-19 01 48.7	1.8	.004	.001	0.28	0.18	*	*	*	
76	1XMM J074742.2-190226	07 47 42.20	-19 02 25.6	2.8	.004	.001	-0.78	0.12	*	*	*	
51	1XMM J074819.5-191110	07 48 19.53	-19 11 09.7	3.4	.004	.001	-0.06	0.17	*	*	*	
83	1XMM J074751.2-185629	07 47 51.22	-18 56 29.5	2.9	.004	.001	0.06	0.26	*	*	*	
95	1XMM J074746.8-190443	07 47 46.75	-19 04 43.4	3.4	.004	.001	-1.00	0.14	*	*	*	
50	1XMM J074752.6-185714	07 47 52.56	-18 57 13.6	2.6	.004	.001	-0.33	0.18	*	*	*	
38	1XMM J074758.8-190603	07 47 58.75	-19 06 02.6	2.0	.004	.001	-0.56	0.15	EG	21.27	AGN	
35	1XMM J074802.6-190760	07 48 02.64	-19 08 00.0	2.4	.004	.001	-0.05	0.19	*	*	*	
42	1XMM J074821.3-191510	07 48 21.32	-19 15 09.9	2.3	.004	.001	-1.00	0.19	AC	15.02	G1V	S102202322264 GSC2
72	1XMM J074854.1-185628	07 48 54.07	-18 56 28.2	3.3	.004	.001	-0.55	0.21	*	*	*	
60	1XMM J074735.8-190555	07 47 35.80	-19 05 55.2	2.9	.004	.001	-0.38	0.29	EG	22.52	Gal	
31	1XMM J074802.4-190252	07 48 02.39	-19 02 51.6	1.8	.004	.001	-0.25	0.15	AC	16.46	G4V	S102202332109 GSC2
32	1XMM J074812.7-191004	07 48 12.73	-19 10 04.4	3.3	.003	.000	0.10	0.20	*	*	*	
27	1XMM J074846.8-190338	07 48 46.79	-19 03 38.3	1.9	.003	.001	-0.35	0.16	EG	19.80	Gal	
59	1XMM J074828.8-191245	07 48 28.84	-19 12 45.3	2.3	.003	.001	-0.61	0.18	EG	24.42	Gal	
49	1XMM J074908.7-185954	07 49 08.75	-18 59 54.5	2.4	.003	.001	-0.18	0.22	*	*	*	
52	1XMM J074813.0-185920	07 48 13.05	-18 59 20.4	2.1	.003	.001	0.01	0.21	*	*	*	
79	1XMM J074829.4-185645	07 48 29.37	-18 56 45.2	2.4	.003	.001	-0.35	0.23	*	*	*	
34	1XMM J074844.4-190756	07 48 44.41	-19 07 55.6	2.0	.003	.000	-0.17	0.17	*	*	*	
64	1XMM J074757.2-190244	07 47 57.22	-19 02 44.0	2.5	.003	.001	0.07	0.20	*	*	*	
45	1XMM J074804.6-190814	07 48 04.59	-19 08 13.7	1.8	.003	.001	-0.05	0.20	EG	21.20	AGN	
99	1XMM J074822.4-185416	07 48 22.43	-18 54 15.5	6.6	.003	.001	-0.59	0.21	*	*	*	
70	1XMM J074828.6-191414	07 48 28.61	-19 14 14.0	2.9	.002	.001	-0.28	0.26	AC	*	G7V	TYC 5989-84-1
43	1XMM J074821.9-190256	07 48 21.87	-19 02 55.6	2.1	.002	.000	-0.34	0.18	AC	20.33	Me	

68	1XMM J074802.4-185746	07 48 02.44	-18 57 46.2	4.3	.002	.001	0.99	0.25	EG	20.80	Gal	
41	1XMM J074802.3-185820	07 48 02.34	-18 58 19.5	3.6	.002	.001	-1.00	0.13	AC	13.13	F6V	S1022023360 GSC2
44	1XMM J074826.5-190216	07 48 26.51	-19 02 16.5	2.2	.002	.000	-0.45	0.18	AC	16.06	F7V	S102202332619 GSC2
57	1XMM J074823.1-191408	07 48 23.13	-19 14 07.5	3.0	.002	.001	-0.39	0.21	EG	20.12	AGN	
55	1XMM J074839.5-191303	07 48 39.53	-19 13 02.8	2.3	.002	.001	0.70	0.18	EG	19.71	Gal	
39	1XMM J074814.5-190538	07 48 14.50	-19 05 37.7	2.6	.002	.000	-0.43	0.20	EG	20.91	AGN	
75	1XMM J074812.5-191107	07 48 12.47	-19 11 06.6	6.0	.002	.000	1.00	2.21	*			
86	1XMM J074851.5-190746	07 48 51.47	-19 07 46.3	3.9	.002	.000	-1.00	0.18	AC	14.59	K4V	S102202212384 GSC2
78	1XMM J074818.1-190656	07 48 18.11	-19 06 56.2	3.4	.002	.000	-0.55	0.30	*			
69	1XMM J074820.8-190716	07 48 20.76	-19 07 15.6	3.5	.001	.000	-0.28	0.21	EG	19.73	Gal	
63	1XMM J074822.0-190806	07 48 22.03	-19 08 06.1	2.6	.001	.000	-0.59	0.19	AC	12.93	G9V	S102202328312 GSC2
87	1XMM J074802.1-185952	07 48 02.13	-18 59 52.3	3.0	.001	.000	0.61	0.24	*			

Table 12. GRB 001025

Src Num	Source Name	RA (J2000)	DEC (J2000)	r90 arcsec	pn countrate cts/s	error cts/s	pn HR2	pn HR2 error	Class	R	Type	Optical Id
1	1XMM J083611.3-125840	08 36 11.34	-12 58 40.0	1.1	.095	.003	-0.61	0.03	EG	18.48	AGN	GSC S13132027472
2	1XMM J083616.4-130949	08 36 16.37	-13 09 49.3	1.3	.042	.002	-0.89	0.03	ACe	15.35	Me	GSC S13132023854
15	1XMM J083647.1-131653	08 36 47.08	-13 16 52.9	1.7	.017	.002	-0.57	0.09	EG	19.06	NELG	USNO-B1 0767-0199056
72	1XMM J083721.4-125720	08 37 21.42	-12 57 19.9	1.4	.017	.006	-1.00	0.23	EG	19.75	AGN	USNO-B1 0770-0229958
16	1XMM J083546.1-125459	08 35 46.15	-12 54 58.8	2.6	.016	.002	-0.81	0.08	*	*	*	*
11	1XMM J083606.9-125347	08 36 06.94	-12 53 46.7	1.6	.015	.002	-0.68	0.10	EG	20.55	AGN	USNO-B1 0771-0239448
14	1XMM J083652.9-131514	08 36 52.88	-13 15 14.3	1.5	.014	.002	-0.27	0.12	*	*	*	*
5	1XMM J083601.0-130035	08 36 00.98	-13 00 34.8	1.6	.013	.001	-0.54	0.09	*	*	*	*
29	1XMM J083708.9-130229	08 37 08.90	-13 02 29.3	1.7	.013	.002	-0.75	0.14	*	*	*	*
28	1XMM J083538.7-130356	08 35 38.68	-13 03 55.9	2.7	.013	.002	-0.60	0.10	AC	16.08	*	GSC S13132036888
27	1XMM J083546.3-130910	08 35 46.28	-13 09 10.0	1.8	.013	.003	-0.60	0.17	*	*	*	*
38	1XMM J083542.7-125717	08 35 42.65	-12 57 16.5	4.7	.012	.002	-0.72	0.12	*	*	*	*
8	1XMM J083704.1-125524	08 37 04.12	-12 55 24.1	1.7	.012	.001	-0.65	0.08	*	*	*	*
4	1XMM J083632.7-125615	08 36 32.74	-12 56 15.2	1.5	.011	.001	-0.69	0.07	*	*	*	*
7	1XMM J083615.4-130110	08 36 15.36	-13 01 10.3	1.7	.009	.001	-0.57	0.09	*	*	*	*
10	1XMM J083616.7-130743	08 36 16.68	-13 07 43.2	1.9	.009	.001	-0.61	0.10	*	*	*	*
9	1XMM J083635.7-130105	08 36 35.74	-13 01 04.9	1.5	.009	.001	-0.70	0.07	*	*	*	*
24	1XMM J083556.7-131015	08 35 56.67	-13 10 14.6	2.9	.008	.001	-0.74	0.12	*	*	*	*
18	1XMM J083629.3-130924	08 36 29.29	-13 09 24.1	1.9	.008	.001	-0.51	0.10	*	*	*	*
6	1XMM J083627.2-130343	08 36 27.23	-13 03 42.9	1.5	.008	.001	-0.84	0.05	*	*	*	*
46	1XMM J083700.9-131703	08 37 00.87	-13 17 02.6	4.2	.008	.002	-0.26	0.16	ACe	15.74	FG	GSC S13132021935
20	1XMM J083615.2-125720	08 36 15.18	-12 57 20.3	2.5	.008	.001	-0.54	0.11	*	*	*	*
12	1XMM J083624.2-125920	08 36 24.21	-12 59 19.6	1.7	.007	.001	-0.64	0.08	EG	20.30	AGN	USNO-B1 0770-0229459
30	1XMM J083715.1-130922	08 37 15.05	-13 09 22.3	2.1	.007	.001	-0.69	0.12	*	*	*	*
17	1XMM J083646.4-125930	08 36 46.38	-12 59 30.0	1.8	.007	.001	-0.70	0.08	*	*	*	*
36	1XMM J083605.8-125321	08 36 05.81	-12 53 20.7	3.1	.007	.002	-0.31	0.14	EG	19.38	AGN	USNO-B1 0771-0239435
21	1XMM J083631.2-125728	08 36 31.19	-12 57 28.1	1.5	.007	.001	-0.54	0.12	*	*	*	*
55	1XMM J083603.6-131407	08 36 03.55	-13 14 07.1	3.2	.006	.001	0.20	0.18	*	*	*	*
63	1XMM J083714.0-125655	08 37 14.03	-12 56 55.4	1.8	.006	.001	0.25	0.22	*	*	*	*
45	1XMM J083536.9-130648	08 35 36.87	-13 06 47.7	2.3	.006	.002	-0.84	0.13	*	*	*	*
19	1XMM J083632.2-130719	08 36 32.21	-13 07 19.5	1.6	.006	.001	-0.53	0.15	*	*	*	*
54	1XMM J083604.5-131129	08 36 04.50	-13 11 28.9	3.5	.006	.001	-0.65	0.14	*	*	*	*
77	1XMM J083645.8-125240	08 36 45.81	-12 52 39.9	2.8	.006	.001	-0.16	0.23	*	*	*	*
25	1XMM J083600.2-130728	08 36 00.17	-13 07 28.2	2.3	.006	.001	-0.93	0.08	*	*	*	*
41	1XMM J083639.2-125426	08 36 39.22	-12 54 25.7	2.0	.006	.001	-0.50	0.17	*	*	*	*
23	1XMM J083627.9-130160	08 36 27.85	-13 01 59.7	1.7	.005	.001	-0.57	0.10	EG	20.93	AGN	Object A
22	1XMM J083628.3-130723	08 36 28.29	-13 07 22.9	1.8	.005	.001	-0.46	0.13	*	*	*	*
64	1XMM J083544.2-125742	08 35 44.21	-12 57 42.4	3.7	.005	.002	-0.96	0.17	*	*	*	*
50	1XMM J083546.7-131356	08 35 46.74	-13 13 55.7	3.6	.005	.001	-0.45	0.15	*	*	*	*
80	1XMM J083614.4-125233	08 36 14.44	-12 52 33.0	3.1	.005	.002	-0.39	0.22	*	*	*	*
32	1XMM J083642.0-125841	08 36 42.04	-12 58 41.2	2.6	.005	.001	-0.23	0.18	*	*	*	*
52	1XMM J083716.3-125628	08 37 16.26	-12 56 27.8	2.6	.005	.002	-0.45	0.16	*	*	*	*
33	1XMM J083649.5-125655	08 36 49.48	-12 56 55.4	2.0	.005	.001	-0.68	0.12	*	*	*	*
47	1XMM J083610.3-130714	08 36 10.33	-13 07 14.1	2.8	.005	.001	-0.50	0.24	*	*	*	*
26	1XMM J083615.6-130339	08 36 15.59	-13 03 39.3	2.7	.005	.001	-0.76	0.09	*	*	*	*
74	1XMM J083710.7-125541	08 37 10.69	-12 55 40.7	3.6	.005	.001	-0.21	0.20	*	*	*	*
37	1XMM J083648.9-125730	08 36 48.86	-12 57 30.1	2.7	.004	.001	-1.00	0.64	ACe	17.29	Me	GSC S13132027875
66	1XMM J083715.7-131035	08 37 15.68	-13 10 35.1	3.5	.004	.001	-0.25	0.21	*	*	*	*
39	1XMM J083645.4-130360	08 36 45.43	-13 03 59.6	2.8	.004	.001	0.51	0.19	EG	19.31	NELG	USNO-B1 0769-0217902
31	1XMM J083654.4-130746	08 36 54.38	-13 07 45.7	1.8	.004	.001	-0.36	0.16	*	*	*	*
60	1XMM J083711.0-130143	08 37 11.05	-13 01 42.8	3.9	.004	.001	-0.36	0.19	*	*	*	*
69	1XMM J083623.2-130638	08 36 23.15	-13 06 38.1	2.5	.004	.001	-0.33	0.29	*	*	*	*
58	1XMM J083647.4-125605	08 36 47.38	-12 56 04.8	3.6	.003	.001	-0.70	0.14	*	*	*	*
65	1XMM J083655.8-131043	08 36 55.77	-13 10 42.9	2.8	.003	.001	-0.57	0.22	*	*	*	*
48	1XMM J083649.8-130929	08 36 49.78	-13 09 28.8	3.3	.003	.001	-0.58	0.15	*	*	*	*
35	1XMM J083638.0-130819	08 36 38.04	-13 08 19.0	4.4	.003	.001	-0.87	0.11	*	*	*	*
57	1XMM J083650.2-131251	08 36 50.24	-13 12 51.2	2.6	.003	.001	-0.32	0.18	*	*	*	*
67	1XMM J083614.7-130720	08 36 14.67	-13 07 20.0	1.9	.003	.001	-0.47	0.19	*	*	*	*
43	1XMM J083620.1-130511	08 36 20.12	-13 05 10.7	2.1	.003	.001	-0.63	0.14	*	*	*	*
34	1XMM J083648.6-130151	08 36 48.56	-13 01 50.6	1.9	.003	.001	-0.53	0.15	ACe	18.08	Me	USNO-B1 0769-0217935

42	1XMM J083622.2-130319	08 36 22.16	-13 03 19.4	2.9	.003	.001	-0.56	0.15	*
56	1XMM J083712.1-131228	08 37 12.09	-13 12 27.8	7.4	.003	.001	0.29	0.32	*
75	1XMM J083627.6-130023	08 36 27.61	-13 00 22.6	3.9	.003	.001	0.18	0.20	*
70	1XMM J083656.0-130537	08 36 55.96	-13 05 36.8	5.2	.003	.001	-0.61	0.57	*
49	1XMM J083637.7-131041	08 36 37.74	-13 10 41.2	6.3	.003	.001	-1.00	0.32	*
68	1XMM J083629.9-131024	08 36 29.87	-13 10 23.8	2.6	.003	.001	0.72	0.28	*
44	1XMM J083618.4-130118	08 36 18.41	-13 01 18.3	2.5	.003	.001	-0.97	0.12	*
53	1XMM J083720.4-130340	08 37 20.38	-13 03 40.2	2.9	.003	.001	-0.87	0.17	*
40	1XMM J083629.7-130103	08 36 29.73	-13 01 02.8	3.3	.003	.001	-0.46	0.15	*
83	1XMM J083642.3-130026	08 36 42.35	-13 00 26.5	4.4	.002	.001	-0.72	0.34	*
51	1XMM J083651.2-130437	08 36 51.19	-13 04 36.8	2.4	.002	.000	-0.92	0.17	*
78	1XMM J083701.6-130611	08 37 01.63	-13 06 10.5	3.6	.002	.001	-0.76	0.15	*

Table 13. GRO J 1655-40

Src Num	Source Name	RA (J2000)	DEC (J2000)	r90 arcsec	pn countrate cts/s	error cts/s	pn HR2	pn HR2 error	Class	R	Type	Optical Id
48	XMMU J165515.6-394544	16 55 15.61	-39 45 44.8	2.0	.060	.004	-0.64	0.05	ACe	14.76	K4Ve	GSC2 S230322140806
10	XMMU J165341.2-395734	16 53 41.18	-39 57 34.7	1.6	.024	.002	-0.04	0.08	AC	17.40		
12	XMMU J165340.1-395709	16 53 40.10	-39 57 09.1	1.8	.019	.002	0.04	0.10	AC	18.25		
40	XMMU J165443.0-394803	16 54 43.01	-39 48 03.4	1.8	.019	.002	-0.54	0.07	AC	13.00	A7V	USNOA2 0450-25955452
52	XMMU J165310.5-394449	16 53 10.45	-39 44 49.3	1.7	.018	.002	-0.60	0.08	AC	13.28	K1V	GSC2 S230322140934
34	XMMU J165438.1-400146	16 54 38.15	-40 01 46.7	2.2	.013	.002	-0.66	0.11	AC	14.65	G7V	GSC2 S230322135512
41	XMMU J165325.7-394815	16 53 25.70	-39 48 15.1	1.8	.012	.001	0.15	0.12	AC	17.20		
13	XMMU J165304.3-395558	16 53 04.26	-39 55 58.6	2.6	.012	.002	-0.88	0.10	AC	12.07	M2V	GSC S230322138167
59	XMMU J165445.0-394053	16 54 44.99	-39 40 53.7	4.5	.010	.002	0.02	0.19	*			
58	XMMU J165410.6-394203	16 54 10.55	-39 42 03.6	2.4	.010	.002	-0.94	0.09	ACe	14.85	K1Ve	GSC2 S230322141287
7	XMMU J165508.4-395917	16 55 08.35	-39 59 17.0	9.5	.010	.003	0.91	0.30	*			
19	XMMU J165511.7-395324	16 55 11.66	-39 53 24.4	9.3	.010	.002	-1.00	1.21	*			
1	XMMU J165445.0-400229	16 54 45.04	-40 02 29.0	6.7	.010	.002	-0.85	0.16	*			
25	XMMU J165518.8-395301	16 55 18.80	-39 53 01.0	7.3	.009	.002	-1.00	0.07	*			
57	XMMU J165500.3-394205	16 55 00.27	-39 42 05.3	4.9	.009	.002	-0.83	0.17	AC	*		TYC 7872-1109-1
2	XMMU J165454.6-400137	16 54 54.58	-40 01 37.5	9.5	.008	.003	0.66	0.40	*			
21	XMMU J165314.8-395310	16 53 14.83	-39 53 10.0	2.3	.008	.001	-0.95	0.08	ACe	15.78	K4Ve	GSC2 S230322139158
60	XMMU J165421.8-393939	16 54 21.79	-39 39 39.4	4.1	.008	.002	-0.28	0.17	*			
17	XMMU J165301.0-395414	16 53 01.02	-39 54 14.7	2.7	.008	.001	-0.38	0.15	*			
62	XMMU J165425.5-393758	16 54 25.49	-39 37 58.7	7.1	.008	.002	-1.00	0.40	*			
44	XMMU J165440.5-394705	16 54 40.54	-39 47 05.6	2.6	.007	.001	-0.61	0.12	AC	15.20	G9V	GSC2 S230322140569
61	XMMU J165402.5-393818	16 54 02.49	-39 38 18.8	3.9	.006	.002	-0.17	0.21	*			
15	XMMU J165449.4-395450	16 54 49.39	-39 54 50.9	6.0	.006	.002	-0.16	0.29	AC	12.91	G6V+A	GSC2 S230322138660
5	XMMU J165334.1-400004	16 53 34.10	-40 00 04.8	2.7	.006	.002	-0.68	0.17	AC	*	F5	HD 322240
55	XMMU J165458.0-394230	16 54 57.98	-39 42 30.7	8.7	.006	.002	-0.31	0.31	*			
4	XMMU J165326.2-393914	16 53 26.19	-39 39 14.4	5.9	.006	.002	0.11	0.24	*			
9	XMMU J165420.2-395831	16 54 20.23	-39 58 31.9	3.3	.006	.001	0.19	0.20	AC	16.70		USNOA2 0450-25937532
6	XMMU J165426.6-395915	16 54 26.58	-39 59 15.6	3.5	.005	.001	-1.00	0.58	*			
46	XMMU J165402.0-394630	16 54 01.98	-39 46 30.1	3.1	.005	.001	0.36	0.38	EG	*	AGN	NVSS J165402-394630
47	XMMU J165503.0-394623	16 55 02.96	-39 46 23.6	8.1	.005	.002	-0.13	0.38	*			
37	XMMU J165339.0-400216	16 53 38.98	-40 02 16.8	6.0	.005	.002	0.27	0.35	*			
31	XMMU J165426.8-395103	16 54 26.80	-39 51 03.9	2.8	.005	.001	-0.02	0.17	EG	*	Radio	NVSS J165426-395106
14	XMMU J165315.0-395508	16 53 15.04	-39 55 08.2	4.5	.005	.001	-0.93	0.14	*			
36	XMMU J165452.0-394915	16 54 51.97	-39 49 15.9	8.9	.005	.001	0.13	1.07	*			
53	XMMU J165349.3-394356	16 53 49.34	-39 43 56.8	5.5	.005	.001	-0.50	0.24	AC	14.34		GSC2 S230322141062
32	XMMU J165505.1-395058	16 55 05.12	-39 50 58.0	8.3	.005	.002	0.02	0.54	*			
56	XMMU J165423.9-394223	16 54 23.87	-39 42 23.7	3.9	.005	.001	-0.64	0.30	*			
45	XMMU J165421.2-394635	16 54 21.19	-39 46 35.3	3.0	.005	.001	-0.50	0.15	AC	15.86	K0V	GSC2 S230322140651
49	XMMU J165407.2-394601	16 54 07.23	-39 46 01.2	2.8	.005	.001	-1.00	0.04	AC	11.90	F3V	GSC2 S2303221325
22	XMMU J165416.9-400149	16 54 16.85	-40 01 49.2	10.	.005	.002	*	*	*			
18	XMMU J165327.7-395406	16 53 27.72	-39 54 06.8	5.1	.004	.001	-0.28	0.24	*			
54	XMMU J165400.0-394254	16 54 00.03	-39 42 54.2	7.2	.004	.001	-0.29	0.44	*			
11	XMMU J165346.4-395723	16 53 46.41	-39 57 23.5	4.0	.004	.001	0.17	0.26	*			
42	XMMU J165418.3-394805	16 54 18.34	-39 48 05.7	4.4	.004	.001	0.19	0.24	*			
16	XMMU J165412.3-395435	16 54 12.29	-39 54 35.0	2.9	.004	.001	-1.00	0.06	AC	15.72	K0V	GSC2 S230322138715
43	XMMU J165320.7-394745	16 53 20.71	-39 47 45.3	4.3	.004	.001	0.05	0.26	*			
26	XMMU J165421.7-395240	16 54 21.70	-39 52 40.8	4.5	.003	.001	-0.24	0.26	*			
50	XMMU J165346.3-394556	16 53 46.27	-39 45 56.4	4.4	.003	.001	-0.07	0.23	*			
38	XMMU J165440.6-394913	16 54 40.59	-39 49 13.0	5.7	.003	.001	-1.00	0.24	AC	14.50	F5V	USNOA2 0450-25953271
8	XMMU J165353.3-395921	16 53 53.31	-39 59 21.1	6.8	.003	.001	-1.00	0.13	*			
24	XMMU J165402.1-395307	16 54 02.07	-39 53 07.4	3.7	.003	.001	0.53	0.23	AC	16.20		GSC2 S230322139195
39	XMMU J165423.4-394911	16 54 23.39	-39 49 11.9	5.2	.003	.001	1.00	0.84	*			
3	XMMU J165357.3-400128	16 53 57.34	-40 01 28.2	8.9	.003	.001	-0.30	0.33	*			
35	XMMU J165451.1-395018	16 54 51.07	-39 50 18.2	8.0	.003	.001	0.16	0.74	*			
23	XMMU J165421.8-395309	16 54 21.83	-39 53 09.4	4.8	.003	.001	-0.39	0.22	AC	17.01		GSC2 S230322118717
30	XMMU J165440.4-395112	16 54 40.40	-39 51 12.4	7.5	.003	.001	0.69	0.65	*			
20	XMMU J165335.2-395318	16 53 35.23	-39 53 18.3	6.0	.003	.001	-1.00	0.11	*			
28	XMMU J165426.9-395227	16 54 26.92	-39 52 27.5	4.6	.003	.001	-0.28	0.22	AC	16.39		GSC2 S230322119313
29	XMMU J165355.0-395131	16 53 55.03	-39 51 31.3	8.1	.002	.001	0.15	0.35	*			
27	XMMU J165411.3-395236	16 54 11.33	-39 52 36.9	5.4	.002	.001	-0.57	0.27	AC	15.86		GSC2 S230322139361

51	XMMU J165404.2-394539	16 54 04.15	-39 45 40.0	13.	.001	.001	*	*	*
----	-----------------------	-------------	-------------	-----	------	------	---	---	---

Table 14. GC 2

Src Num	Source Name	RA (J2000)	DEC (J2000)	r90 arcsec	pn countrate cts/s	error cts/s	pn HR2	pn HR2 error	Class	R	Type	Optical Id
1	1XMM J174705.4-280900	17 47 05.36	-28 09 00.4	1.1	.167	.004	-0.79	0.02	AC	*	F3V	HD 161507
2	1XMM J174722.8-280906	17 47 22.82	-28 09 06.2	1.2	.117	.004	0.98	0.02	SNR	*	SNR	SNR 000.9+00.1
3	1XMM J174645.4-281548	17 46 45.37	-28 15 48.0	2.3	.070	.005	0.98	0.02		*		
6	1XMM J174817.0-280748	17 48 16.97	-28 07 48.0	1.5	.039	.004	0.62	0.10	AC	17.20		USNOA20600-28829561
4	1XMM J174654.7-281657	17 46 54.71	-28 16 57.2	1.3	.037	.003	-0.47	0.07	AC	14.60	GOVe	GSC2 S222131216860
13	1XMM J174814.1-281620	17 48 14.06	-28 16 19.9	1.8	.025	.004	1.00	0.14		*		
7	1XMM J174631.2-281029	17 46 31.24	-28 10 29.4	1.5	.022	.003	-0.72	0.09	AC	12.27	K1V	GSC2 S222131224069
30	1XMM J174709.8-281111	17 47 09.84	-28 11 11.3	2.4	.022	.005	1.00	0.49		*		
5	1XMM J174717.7-281027	17 47 17.73	-28 10 26.7	1.4	.019	.002	0.83	0.10		*		
10	1XMM J174732.3-280854	17 47 32.26	-28 08 54.5	1.6	.011	.001	1.00	0.07		*		
19	1XMM J174654.3-280302	17 46 54.28	-28 03 02.1	2.2	.010	.001	0.56	0.17		*		
11	1XMM J174756.1-280509	17 47 56.14	-28 05 09.0	1.7	.009	.002	-0.17	0.13		*		
39	1XMM J174828.3-280929	17 48 28.30	-28 09 29.4	3.7	.009	.002	0.69	0.26		*		
45	1XMM J174819.8-280728	17 48 19.76	-28 07 28.1	3.2	.009	.002	-0.12	0.30	AC	13.96		GSC2 S222131226529
9	1XMM J174730.9-281347	17 47 30.89	-28 13 46.7	1.9	.009	.001	-1.00	0.04	ACe	16.72	M5Ve	
15	1XMM J174802.1-281709	17 48 02.10	-28 17 09.5	2.0	.008	.002	-0.86	0.11	ACe	14.91	M4Ve	USNOB1 0617-0637905
43	1XMM J174803.9-281446	17 48 03.94	-28 14 45.5	2.9	.008	.002	0.02	0.34	ACe	19.50	M5Ve	USNOB1 0617-0637929
18	1XMM J174748.3-280357	17 47 48.30	-28 03 57.0	2.6	.008	.001	1.00	0.21		*		
16	1XMM J174746.6-280903	17 47 46.57	-28 09 02.8	2.6	.007	.001	0.29	0.30		*		
17	1XMM J174712.0-280956	17 47 12.02	-28 09 56.0	1.7	.007	.001	0.29	0.28	AC	17.47	F5V+K	USNOB1 0618-0682596
14	1XMM J174714.7-280614	17 47 14.73	-28 06 14.0	2.0	.007	.001	-0.80	0.10	AC	14.43	G7V	GSC2 S222131227712
20	1XMM J174733.1-282105	17 47 33.10	-28 21 04.9	4.1	.006	.002	-1.00	0.19	AC	13.90		USNOB1 0616-0602189
27	1XMM J174647.4-281108	17 46 47.40	-28 11 07.6	4.5	.006	.001	1.00	1.04		*		
63	1XMM J174810.9-281829	17 48 10.88	-28 18 28.8	4.8	.006	.002	-0.89	0.13	AC	*		TYC 6840-929-1
26	1XMM J174652.1-280914	17 46 52.09	-28 09 13.7	3.2	.006	.001	0.25	0.21	AC	16.46	F9V	GSC2 S222131225135
22	1XMM J174743.2-281307	17 47 43.24	-28 13 06.7	3.8	.006	.001	1.00	3.89		*		
34	1XMM J174658.7-281419	17 46 58.66	-28 14 19.5	3.4	.005	.001	1.00	0.39	AC	15.07		GSC2 S222131219989
24	1XMM J174746.2-280654	17 47 46.16	-28 06 54.3	3.2	.005	.001	-0.09	0.45		*		
21	1XMM J174729.9-281305	17 47 29.88	-28 13 05.2	2.4	.005	.001	-0.63	0.12	AC	15.86	G9V	GSC2 S222131221179
48	1XMM J174734.6-281834	17 47 34.61	-28 18 34.3	2.8	.005	.001	-0.86	0.21		*		
66	1XMM J174657.1-281343	17 46 57.09	-28 13 42.7	5.3	.004	.001	1.00	0.13		*		
25	1XMM J174707.7-280123	17 47 07.75	-28 01 22.7	2.4	.004	.001	-0.92	0.14	AC	12.63	K3V	GSC2 S222131231922
33	1XMM J174720.8-281321	17 47 20.82	-28 13 21.5	4.4	.004	.001	0.79	0.27		*		
28	1XMM J174746.0-280732	17 47 45.97	-28 07 32.4	3.1	.004	.001	-0.49	0.18		*		
44	1XMM J174735.7-282013	17 47 35.69	-28 20 13.0	2.3	.004	.002	-0.75	0.16	AC	15.98		GSC2 S222131212417
54	1XMM J174653.2-280205	17 46 53.18	-28 02 04.7	5.9	.004	.001	1.00	0.60		*		
31	1XMM J174733.6-281402	17 47 33.59	-28 14 02.4	2.7	.004	.001	1.00	0.37		*		
36	1XMM J174726.8-281702	17 47 26.75	-28 17 02.2	2.7	.003	.001	-0.91	0.14	ACe	16.58	M1Ve	GSC2 S222131216600
32	1XMM J174717.7-275837	17 47 17.69	-27 58 36.9	2.3	.003	.001	-0.62	0.18	ACe	15.10	K1V	GSC2 S222131233929
51	1XMM J174736.8-281442	17 47 36.76	-28 14 42.2	2.4	.002	.001	-0.50	0.17	AC	13.45	F9V	GSC2 S222131219308

Table 15. WR 110

Src Num	Source Name	RA (J2000)	DEC (J2000)	r90 arcsec	pn countrate cts/s	error cts/s	pn HR2	pn HR2 error	Class	R	Type	Optical Id
3	1XMM J180706.8-192600	18 07 06.82	-19 26 00.2	1.2	.041	.002	-0.95	0.02	ACe	13.16	M1	GSC S30010332115
2	1XMM J180802.2-191506	18 08 02.17	-19 15 06.4	1.2	.031	.002	-0.73	0.04	AC	12.94	K1	GSC S30010334782
6	1XMM J180712.7-191333	18 07 12.66	-19 13 33.1	2.1	.030	.004	-0.95	0.03	AC	*	G6	Bright Star A
4	1XMM J180736.4-192657	18 07 36.42	-19 26 57.5	1.2	.023	.001	-0.12	0.06	AC	15.11	G8	GSC S300103216580
5	1XMM J180822.4-191813	18 08 22.43	-19 18 12.5	1.3	.017	.001	-0.73	0.06	AC	14.09	K2	GSC S300103223953
11	1XMM J180749.5-192606	18 07 49.51	-19 26 06.5	1.3	.014	.001	-0.92	0.05	AC	13.63	G8	GSC S300103217225
8	1XMM J180804.4-192453	18 08 04.43	-19 24 52.5	1.3	.014	.001	-0.39	0.08	ACe	18.56	K3III	Star A
16	1XMM J180713.4-191729	18 07 13.39	-19 17 29.1	1.6	.011	.002	-1.00	0.08	AC	*	F5V	HD 165552
10	1XMM J180741.5-191700	18 07 41.47	-19 17 00.2	1.5	.010	.001	0.81	0.10	*	*	*	*
7	1XMM J180804.3-191705	18 08 04.27	-19 17 05.3	1.6	.009	.001	-0.96	0.03	AC	12.66	F3	GSC S30010334316
13	1XMM J180722.6-192037	18 07 22.61	-19 20 37.5	1.6	.009	.001	-0.87	0.05	AC	15.03	G9	GSC S30010333407
14	1XMM J180723.4-192406	18 07 23.43	-19 24 06.3	1.7	.008	.001	-0.26	0.12	*	*	*	*
21	1XMM J180738.3-193216	18 07 38.26	-19 32 15.7	1.9	.008	.001	0.38	0.15	ACe	19.59	M3e	Star A
34	1XMM J180656.3-192248	18 06 56.32	-19 22 47.8	2.5	.008	.002	-1.00	0.08	AC	*	F6	HD 165481
25	1XMM J180713.2-192707	18 07 13.23	-19 27 07.0	2.0	.007	.001	0.51	0.23	*	*	*	*
23	1XMM J180822.3-192834	18 08 22.34	-19 28 33.6	2.2	.007	.001	0.49	0.23	*	*	*	*
39	1XMM J180737.8-191408	18 07 37.84	-19 14 08.0	3.6	.007	.001	0.43	0.16	*	*	*	*
17	1XMM J180748.7-191835	18 07 48.65	-19 18 34.6	1.7	.007	.001	0.76	0.09	*	*	*	*
29	1XMM J180727.8-193225	18 07 27.76	-19 32 25.1	2.2	.006	.001	-0.88	0.09	*	*	*	*
38	1XMM J180701.9-192042	18 07 01.87	-19 20 41.7	3.8	.006	.001	-0.70	0.11	AC	16.72	K0	Star B
41	1XMM J180758.8-193650	18 07 58.77	-19 36 49.6	5.6	.006	.001	-0.80	0.11	AC	*	K0	GSC S300103219
24	1XMM J180733.4-193045	18 07 33.36	-19 30 44.9	1.9	.006	.001	0.79	0.19	*	*	*	*
19	1XMM J180814.5-192660	18 08 14.51	-19 26 59.8	1.8	.006	.001	-0.79	0.06	ACe	17.50	M3e	*
59	1XMM J180658.1-192723	18 06 58.13	-19 27 23.5	3.7	.005	.001	-0.40	0.19	*	*	*	*
15	1XMM J180758.6-192311	18 07 58.59	-19 23 11.1	1.9	.005	.001	0.46	0.26	*	*	*	*
64	1XMM J180842.7-192305	18 08 42.70	-19 23 04.8	4.4	.005	.001	-0.03	0.27	*	*	*	*
51	1XMM J180742.8-193718	18 07 42.81	-19 37 17.7	5.0	.005	.001	1.00	3.52	*	*	*	*
57	1XMM J180830.0-192714	18 08 30.04	-19 27 14.3	4.4	.005	.001	-0.11	0.27	*	*	*	*
67	1XMM J180656.4-192706	18 06 56.36	-19 27 06.0	3.8	.005	.002	-1.00	0.23	*	*	*	*
65	1XMM J180748.7-192036	18 07 48.69	-19 20 35.8	1.8	.005	.001	-0.46	0.16	*	*	*	*
45	1XMM J180822.4-193501	18 08 22.40	-19 35 00.9	3.1	.005	.001	0.49	0.25	*	*	*	*
30	1XMM J180805.5-192305	18 08 05.50	-19 23 05.1	2.2	.004	.001	-0.67	0.11	AC	14.82	A5	GSC S300103219784
22	1XMM J180754.0-192034	18 07 54.03	-19 20 34.0	2.1	.004	.001	0.29	0.20	*	*	*	*
43	1XMM J180732.4-191948	18 07 32.37	-19 19 47.8	2.4	.004	.001	-0.58	0.17	AC	17.20	K0	GSC S30010333572
48	1XMM J180819.6-191407	18 08 19.58	-19 14 07.4	3.6	.004	.001	-0.83	0.16	AC	14.84	K0	GSC S30010335058 (A)
33	1XMM J180816.8-191940	18 08 16.78	-19 19 39.6	1.9	.004	.001	0.07	0.18	Be/X	22.06	*	Star B
56	1XMM J180808.8-193553	18 08 08.83	-19 35 52.9	4.3	.004	.001	-0.77	0.13	*	*	*	*
40	1XMM J180722.2-191445	18 07 22.20	-19 14 44.6	3.5	.004	.001	-0.79	0.13	AC	15.03	K2	GSC S30010334839 (A)
36	1XMM J180803.7-192743	18 08 03.73	-19 27 43.3	2.4	.004	.001	-0.41	0.14	ACe	20.80	M4e	Star B
49	1XMM J180721.0-191857	18 07 20.99	-19 18 56.6	2.3	.004	.001	-0.73	0.12	AC	12.40	K0	Star B
32	1XMM J180752.8-192623	18 07 52.85	-19 26 22.9	1.9	.003	.001	-0.88	0.10	AC	12.47	A2	GSC S30010324
79	1XMM J180722.0-192457	18 07 22.05	-19 24 56.9	5.0	.003	.001	0.57	0.28	*	*	*	*
69	1XMM J180828.3-193141	18 08 28.25	-19 31 40.8	5.9	.003	.001	0.27	0.38	*	*	*	*
31	1XMM J180733.3-192644	18 07 33.27	-19 26 44.4	3.3	.003	.001	-0.80	0.14	*	*	*	*
42	1XMM J180735.0-192160	18 07 34.95	-19 21 59.6	2.5	.003	.001	0.71	0.26	*	*	*	*
37	1XMM J180739.4-192346	18 07 39.36	-19 23 46.0	2.7	.003	.001	-0.83	0.09	ACe	19.80	M5e	Star A
53	1XMM J180806.8-192450	18 08 06.77	-19 24 50.2	3.1	.003	.001	-0.41	0.22	*	*	*	*
47	1XMM J180739.6-192038	18 07 39.63	-19 20 37.8	2.5	.003	.001	-0.75	0.11	AC	15.84	K1	GSC S30010333390 (A)
77	1XMM J180745.0-193307	18 07 45.04	-19 33 06.7	3.4	.003	.001	-1.00	0.24	*	*	*	*
63	1XMM J180653.3-191842	18 06 53.34	-19 18 42.5	5.5	.003	.002	-0.94	0.14	*	*	*	*
61	1XMM J180819.6-192253	18 08 19.58	-19 22 52.9	2.4	.002	.001	0.41	0.25	*	*	*	*
81	1XMM J180812.3-192500	18 08 12.26	-19 25 00.1	2.8	.002	.001	-0.79	0.15	*	*	*	*
52	1XMM J180756.1-193204	18 07 56.10	-19 32 03.9	8.0	.002	.001	-1.00	0.07	*	*	*	*
46	1XMM J180825.7-192033	18 08 25.65	-19 20 32.9	4.0	.002	.001	1.00	2.44	*	*	*	*
68	1XMM J180803.0-192523	18 08 03.01	-19 25 23.2	4.4	.002	.001	-0.85	0.12	*	*	*	*
72	1XMM J180809.5-192411	18 08 09.45	-19 24 10.7	4.4	.002	.000	-0.66	0.14	*	*	*	*
58	1XMM J180724.9-191921	18 07 24.87	-19 19 20.7	5.4	.002	.001	-1.00	0.14	*	*	*	*
75	1XMM J180739.1-192955	18 07 39.08	-19 29 54.8	4.7	.002	.001	-0.92	0.20	*	*	*	*
87	1XMM J180739.7-192502	18 07 39.73	-19 25 01.6	8.2	.002	.001	-0.07	0.27	*	*	*	*

71	1XMM J180831.2-192329	18 08 31.23	-19 23 29.1	2.7	.001	.001	*	*	*
----	-----------------------	-------------	-------------	-----	------	------	---	---	---

Table 16. Ridge 3

Src Num	Source Name	RA (J2000)	DEC (J2000)	r90 arcsec	pn countrate cts/s	error cts/s	pn HR2	pn HR2 error	Class	R	Type	Optical Id
1	1XMM J182740.6-113954	18 27 40.58	-11 39 54.1	1.4	.048	.004	-0.80	0.06	ACe	20.00	M5e	
2	1XMM J182706.3-112437	18 27 06.25	-11 24 37.4	1.7	.022	.003	0.73	0.12		*		
4	1XMM J182703.8-113713	18 27 03.78	-11 37 12.7	1.6	.022	.003	-0.32	0.13	ACe	17.70		
6	1XMM J182750.7-113548	18 27 50.73	-11 35 48.3	1.8	.015	.002	-0.00	0.15		*		
3	1XMM J182732.3-113358	18 27 32.29	-11 33 58.4	1.5	.015	.002	0.20	0.14	AC	17.00	FG	
9	1XMM J182749.5-113725	18 27 49.55	-11 37 25.4	1.9	.014	.002	0.02	0.16		*		
16	1XMM J182824.9-112721	18 28 24.92	-11 27 21.2	2.4	.013	.002	0.06	0.21		*		
5	1XMM J182744.8-113956	18 27 44.76	-11 39 55.7	2.6	.013	.002	-0.85	0.08	AC	11.47	G8	USNO 0750-13229697
7	1XMM J182728.6-113741	18 27 28.65	-11 37 40.6	1.9	.012	.002	-0.68	0.14	AC	15.20	G3	
8	1XMM J182726.7-112041	18 27 26.69	-11 20 41.0	2.1	.012	.002	-0.53	0.11	AC	15.60	G2	
11	1XMM J182714.7-111813	18 27 14.70	-11 18 12.7	2.3	.012	.002	0.10	0.18	ACe	21.00	M6e	Star B
18	1XMM J182748.9-112133	18 27 48.92	-11 21 33.1	2.9	.008	.002	-0.76	0.13	ACe	17.95	M4e	GSC S30030204873
19	1XMM J182658.4-113300	18 26 58.44	-11 33 00.4	3.9	.008	.002	-0.04	0.17	ACe	16.40	A0	USNO 0750-13193578
17	1XMM J182733.8-114009	18 27 33.79	-11 40 08.9	3.6	.008	.002	-0.73	0.13		*		
10	1XMM J182741.2-112716	18 27 41.16	-11 27 16.1	1.9	.007	.001	-0.62	0.17	AC	16.10	K0	
15	1XMM J182730.6-113511	18 27 30.64	-11 35 11.5	2.6	.007	.001	-0.87	0.15	AC	12.20	A2	GSC S3001110268
12	1XMM J182734.2-112305	18 27 34.23	-11 23 05.1	2.9	.006	.001	-0.57	0.13	ACe	19.50	M5e	USNO 0750-13221246
22	1XMM J182711.3-113258	18 27 11.32	-11 32 58.2	3.8	.005	.001	1.00	0.64		*		
13	1XMM J182819.1-113020	18 28 19.07	-11 30 19.9	6.8	.005	.001	-0.89	0.16		*		

Table 17. Ridge 4

Src Num	Source Name	RA (J2000)	DEC (J2000)	r90 arcsec	pn countrate cts/s	error cts/s	pn HR2	pn HR2 error	Class	R	Type	Optical Id
1	1XMM J182845.7-111712	18 28 45.72	-11 17 11.5	3.2	.343	.013	-0.86	0.02	ACe	11.71	K7V	GSC2.2 S3003020461
2	1XMM J182756.9-110448	18 27 56.92	-11 04 48.3	3.3	.056	.004	0.82	0.05	*	*		
3	1XMM J182827.7-111751	18 28 27.70	-11 17 51.4	3.4	.049	.005	0.60	0.11	*	*		
4	1XMM J182746.3-110252	18 27 46.34	-11 02 51.6	3.4	.027	.004	0.29	0.15	*	*		
8	1XMM J182819.8-111757	18 28 19.76	-11 17 56.7	3.8	.013	.002	0.13	0.18	*	*		
5	1XMM J182813.7-110114	18 28 13.73	-11 01 14.1	4.5	.013	.002	0.36	0.24	*	*		
23	1XMM J182910.3-110304	18 29 10.31	-11 03 04.0	4.5	.013	.003	-0.20	0.17	*	*		
6	1XMM J182807.9-105945	18 28 07.94	-10 59 45.0	3.5	.013	.002	0.27	0.20	*	*		
7	1XMM J182811.8-110439	18 28 11.76	-11 04 38.6	3.7	.012	.002	-0.08	0.21	AC	*	M2	BD-11 4642
10	1XMM J182823.0-105954	18 28 23.01	-10 59 54.0	4.0	.010	.002	1.00	0.59	AC	15.40		GSC2.2 S300302022732
9	1XMM J182757.1-110544	18 27 57.12	-11 05 44.4	3.9	.008	.002	-0.23	0.19	*	*		
18	1XMM J182844.8-111448	18 28 44.80	-11 14 48.0	7.7	.004	.003	*	*	*	*		

Table 18. G 21.5-0.9

Src Num	Source Name	RA (J2000)	DEC (J2000)	r90 arcsec	pn countrate cts/s	error cts/s	pn HR2	pn HR2 error	Class	R	Type	Optical Id
44	XMMU J183220.8-103511	18 32 20.83	-10 35 11.9	1.1	.122	.004	0.92	0.02	EG	*		Cluster of Galaxies
1	XMMU J183328.7-102409	18 33 28.74	-10 24 09.3	1.1	.121	.004	0.04	0.04	Be/X	10.61	B1III	WL 9 in NGC 6649
3	XMMU J183327.7-103523	18 33 27.70	-10 35 23.9	1.1	.102	.003	0.02	0.03	Be/X	11.47	B0V	SS 397
5	XMMU J183316.5-102339	18 33 16.51	-10 23 39.2	1.5	.022	.002	0.83	0.09	*			
4	XMMU J183315.8-102935	18 33 15.78	-10 29 35.4	1.3	.019	.001	0.07	0.08	*			
8	XMMU J183252.2-102900	18 32 52.19	-10 29 00.0	1.5	.018	.002	0.71	0.08	*			
7	XMMU J183260.0-102913	18 33 00.00	-10 29 13.3	1.3	.018	.002	0.17	0.11	*			
48	XMMU J183401.4-102755	18 34 01.44	-10 27 55.0	1.1	.017	.002	0.92	0.09	*			
60	XMMU J183238.3-104907	18 32 38.32	-10 49 07.3	1.1	.016	.002	0.18	0.13	*			
40	XMMU J183228.2-102710	18 32 28.17	-10 27 10.5	1.2	.015	.001	-0.53	0.08	ACe	20.40	M4Ve	Star A
27	XMMU J183223.1-104349	18 32 23.13	-10 43 49.4	1.4	.009	.001	-0.84	0.06	ACe	19.27	M2e	Star A
9	XMMU J183259.9-103626	18 32 59.89	-10 36 26.3	1.1	.009	.001	1.00	0.11	*			
43	XMMU J183211.4-103442	18 32 11.38	-10 34 42.7	1.8	.009	.001	0.00	0.13	*			
10	XMMU J183302.4-104211	18 33 02.37	-10 42 11.0	1.3	.008	.001	-1.00	0.07	AC	10.65	K4V	USNO 0750-13519182
14	XMMU J183336.7-104130	18 33 36.69	-10 41 30.0	1.7	.007	.001	0.01	0.24	*			
6	XMMU J183307.6-102631	18 33 07.55	-10 26 31.3	2.1	.007	.001	1.00	1.91	AC	16.26		USNO 0750-13524781
18	XMMU J183400.2-103927	18 34 00.23	-10 39 27.9	1.3	.006	.001	0.69	0.20	*			
0	XMMU J183350.1-102817	18 33 50.15	-10 28 17.3	1.6	.005	.001	0.11	0.17	*			
15	XMMU J183337.9-104210	18 33 37.92	-10 42 10.4	2.1	.005	.001	1.00	0.52	ACe	15.33	M3Ve	USNO 0750-13561678
42	XMMU J183218.2-102744	18 32 18.18	-10 27 44.1	1.5	.005	.001	-0.61	0.12	*			
41	XMMU J183227.1-102805	18 32 27.11	-10 28 05.9	1.6	.005	.001	-0.80	0.43	*			
16	XMMU J183340.2-104200	18 33 40.24	-10 42 00.2	2.9	.005	.001	0.82	0.19	*			
22	XMMU J183304.5-103729	18 33 04.48	-10 37 29.0	1.1	.004	.001	0.65	0.22	*			
31	XMMU J183238.9-103458	18 32 38.90	-10 34 58.7	1.3	.003	.001	-0.12	0.17	AC	16.38	K2-G7	USNO 0750-13491248
37	XMMU J183239.2-103125	18 32 39.20	-10 31 25.1	2.5	.003	.001	-0.60	0.18	AC	14.90	K0	USNO 0750-13491602
25	XMMU J183258.3-104031	18 32 58.35	-10 40 31.8	3.3	.003	.001	0.02	0.22	*			
39	XMMU J183231.4-103323	18 32 31.41	-10 33 23.8	1.1	.003	.001	-0.62	0.18	AC	17.12		USNO 0750-13482417
23	XMMU J183305.8-104159	18 33 05.77	-10 41 59.5	1.1	.003	.001	0.87	0.21	*			
38	XMMU J183235.7-103150	18 32 35.69	-10 31 50.8	1.6	.003	.001	-0.28	0.20	*			
13	XMMU J183331.5-104027	18 33 31.46	-10 40 27.7	1.1	.003	.001	-1.00	0.22	ACe	14.00	M2Ve	USNO 0750-13553877
28	XMMU J183239.2-104110	18 32 39.16	-10 41 10.0	6.0	.003	.001	0.74	0.27	*			
24	XMMU J183304.0-104207	18 33 03.97	-10 42 07.9	*	.003	.001	-0.88	0.15	AC	*	G5V	HD 171052
29	XMMU J183240.9-103945	18 32 40.88	-10 39 45.8	4.1	.002	.000	-0.23	0.45	*			
30	XMMU J183241.5-103830	18 32 41.53	-10 38 30.3	4.5	.002	.000	0.87	0.42	*			
33	XMMU J183309.0-103507	18 33 09.01	-10 35 07.2	3.7	.001	.000	-1.00	2.06	*			

Table 19. Z And

Src Num	Source Name	RA (J2000)	DEC (J2000)	r90 arcsec	pn countrate cts/s	error cts/s	pn HR2	pn HR2 error	Class	R	Type	Optical Id
2	1XMM J233403.0+485110	23 34 02.96	+48 51 09.8	1.1	.090	.003	-0.50	0.03		*		
3	1XMM J233254.6+484831	23 32 54.59	+48 48 31.3	1.3	.039	.002	-0.59	0.05	NELG	17.75	0.097	USNOA2 1350-18407262
5	1XMM J233327.7+484713	23 33 27.71	+48 47 13.1	1.2	.026	.002	-0.30	0.07		*		
4	1XMM J233307.1+485153	23 33 07.07	+48 51 53.4	1.3	.026	.002	-0.60	0.06		*		
6	1XMM J233341.1+485716	23 33 41.12	+48 57 16.3	1.4	.019	.002	-0.90	0.04	AC	13.82	K0V	USNOA2 1350-18422423
7	1XMM J233500.6+484601	23 35 00.60	+48 46 01.0	1.9	.019	.003	-0.83	0.09	ACe	15.08	M4Ve	USNOA2 1350-18448491
12	1XMM J233412.4+483835	23 34 12.44	+48 38 35.4	1.7	.013	.002	-0.91	0.07	AC	14.21	G0V	USNOA2 1350-18432657
18	1XMM J233431.5+485519	23 34 31.48	+48 55 18.6	1.5	.012	.002	-0.01	0.15		*		
9	1XMM J233338.9+485658	23 33 38.91	+48 56 57.6	1.8	.012	.001	-0.45	0.11		*		
8	1XMM J233326.4+485519	23 33 26.36	+48 55 18.5	1.6	.012	.001	-0.38	0.11		*		
13	1XMM J233236.1+484554	23 32 36.15	+48 45 54.2	1.7	.012	.001	-0.88	0.05		*		
11	1XMM J233401.4+484811	23 34 01.45	+48 48 10.6	1.5	.011	.001	-1.00	0.06	AC	14.10	G5V	USNOA2 1350-18429061
19	1XMM J233444.3+485624	23 34 44.27	+48 56 24.3	1.7	.011	.002	-0.62	0.13		*		
14	1XMM J233405.1+485721	23 34 05.13	+48 57 20.8	1.8	.010	.001	-0.76	0.07	AC	14.14	K0V	USNOA2 1350-18430197
25	1XMM J233244.4+484250	23 32 44.45	+48 42 50.4	1.7	.010	.002	-0.57	0.10		*		
26	1XMM J233230.0+485410	23 32 30.01	+48 54 09.9	2.2	.009	.002	-0.96	0.08		*		
15	1XMM J233245.9+484354	23 32 45.92	+48 43 54.5	2.1	.009	.002	-0.91	0.07	AC	12.57	K0V	USNOA2 1350-18404434
31	1XMM J233447.2+485434	23 34 47.22	+48 54 34.4	2.7	.009	.002	-0.78	0.11	AC	12.90	G1V	USNOA2 1350-18443965
17	1XMM J233326.5+484107	23 33 26.55	+48 41 07.1	1.6	.009	.001	-0.28	0.13		*		
20	1XMM J233342.3+484043	23 33 42.29	+48 40 43.0	1.5	.008	.001	-0.75	0.08		*		
42	1XMM J233222.9+485245	23 32 22.95	+48 52 45.4	4.3	.008	.002	-0.59	0.19		*		
29	1XMM J233349.8+483651	23 33 49.77	+48 36 51.4	2.6	.008	.001	-0.78	0.13	AC	*	K3V	TYC 3641-761-1
10	1XMM J233316.1+484651	23 33 16.13	+48 46 50.7	1.7	.007	.001	-0.86	0.06	ACe	15.62	M4Ve	USNOA2 1350-18414335
21	1XMM J233310.8+485059	23 33 10.77	+48 50 59.4	1.7	.007	.001	-0.47	0.14		*		
16	1XMM J233335.3+485424	23 33 35.29	+48 54 23.5	1.7	.007	.001	-0.83	0.06		*		
40	1XMM J233229.4+484757	23 32 29.43	+48 47 56.8	2.7	.007	.001	-0.30	0.18		*		
37	1XMM J233434.4+485418	23 34 34.43	+48 54 18.3	3.4	.007	.001	-0.62	0.15		*		
24	1XMM J233301.9+484901	23 33 01.91	+48 49 00.5	1.8	.006	.001	-0.08	0.15		*		
35	1XMM J233420.6+484420	23 34 20.61	+48 44 19.7	2.7	.006	.001	-0.66	0.19		*		
23	1XMM J233419.5+485113	23 34 19.48	+48 51 12.7	2.2	.005	.001	-0.81	0.08	AC	15.27	K0V	USNOA2 1350-18434912
32	1XMM J233329.5+490036	23 33 29.52	+49 00 35.8	3.6	.005	.002	-0.71	0.13		*		
41	1XMM J233255.9+484454	23 32 55.89	+48 44 54.0	3.2	.005	.001	-0.32	0.18		*		
44	1XMM J233510.0+485113	23 35 09.99	+48 51 12.8	4.1	.005	.002	-0.88	0.19	AC	*	K2V	TYC 3645-2080-1
28	1XMM J233400.1+485251	23 34 00.10	+48 52 51.4	3.1	.005	.001	-0.41	0.14		*		
33	1XMM J233415.6+484332	23 34 15.59	+48 43 32.5	4.1	.004	.001	0.19	0.22		*		
36	1XMM J233254.5+484244	23 32 54.47	+48 42 43.9	3.8	.004	.001	-0.75	0.12		*		
30	1XMM J233341.5+484731	23 33 41.47	+48 47 31.3	2.4	.004	.001	0.08	0.18		*		
50	1XMM J233350.0+485649	23 33 49.96	+48 56 48.5	4.0	.003	.001	-0.43	0.15		*		
39	1XMM J233317.0+484137	23 33 17.04	+48 41 37.4	6.1	.003	.001	-0.24	0.17		*		
55	1XMM J233320.4+485004	23 33 20.40	+48 50 04.0	2.2	.002	.001	-0.44	0.26		*		

-
- ¹ CNRS, UMR 7550, Observatoire Astronomique de Strasbourg, 11 rue de l'Université, France
- ² Instituto de Física de Cantabria (CSIC-UC), 39005 Santander, Spain
- ³ Mullard Space Science Laboratory, University College London, Holmbury St. Mary, Dorking, RH5 6NT Surrey, UK
- ⁴ Department of Physics and Astronomy, University of Leicester, LE1 7RH, UK
- ⁵ Astrophysikalisches Institut Potsdam, An der Sternwarte 16, 14482 Potsdam, Germany
- ⁶ Max-Planck-Institut für extraterrestrische Physik Giessenbachstraße, 85748 Garching, Germany
- ⁷ Centre d'Etude Spatiale des Rayonnements, 9 Avenue du Colonel Roche, 31028 Toulouse Cedex 4, France